

Post-Newtonian SPH calculations of binary neutron star coalescence. II. Binary mass ratio, equation of state, and spin dependence.

Joshua A. Faber, Frederic A. Rasio, and Justin B. Manor

Department of Physics, Massachusetts Institute of Technology, Cambridge, MA 02139

(February 7, 2008)

Using our new Post-Newtonian SPH (smoothed particle hydrodynamics) code, we study the final coalescence and merging of neutron star (NS) binaries. We vary the stiffness of the equation of state (EOS) as well as the initial binary mass ratio and stellar spins. Results are compared to those of Newtonian calculations, with and without the inclusion of the gravitational radiation reaction. We find a much steeper decrease in the gravity wave peak strain and luminosity with decreasing mass ratio than would be predicted by simple point-mass formulae. For NS with softer EOS (which we model as simple $\Gamma = 2$ polytropes) we find a stronger gravity wave emission, with a different morphology than for stiffer EOS (modeled as $\Gamma = 3$ polytropes as in our previous work). We also calculate the coalescence of NS binaries with an irrotational initial condition, and find that the gravity wave signal is relatively suppressed compared to the synchronized case, but shows a very significant second peak of emission. Mass shedding is also greatly reduced, and occurs via a different mechanism than in the synchronized case. We discuss the implications of our results for gravity wave astronomy with laser interferometers such as LIGO, and for theoretical models of gamma-ray bursts (GRBs) based on NS mergers.

04.30.Db 95.85.Sz 97.60.Jd 47.11.+j 47.75.+f 04.25.Nx

I. INTRODUCTION AND MOTIVATION

Coalescing neutron star (NS) binaries are among the most important sources of gravitational radiation for detection by LIGO [1], VIRGO [2], GEO [3,4], and TAMA [5]. These interferometers will be most sensitive to gravity waves in the frequency range from ~ 10 Hz to ~ 300 Hz, corresponding to the last few thousands of orbits prior to final merging. During final merging, the characteristic frequency is $\gtrsim 1$ kHz, requiring the use of special narrow-band detectors [6], which are currently being tested on the GEO 600 interferometer in Germany [4]. The detection of these merger wave forms, combined with theoretical knowledge about the hydrodynamics of the merger process, could yield detailed information about the behavior of the NS fluid, and, in particular, the EOS of nuclear matter at high density. This is the second of a series of papers in which we attempt to develop this theoretical knowledge using 3D numerical hydrodynamics calculations of NS mergers in post-Newtonian (PN) gravity.

The first Newtonian calculations of binary NS coalescence were performed more than 10 years ago by Nakamura and Oohara using a grid-based Eulerian finite-difference code [7,8]. Rasio and Shapiro (Ref. [9], hereafter RS1–3 or collectively RS) later used Lagrangian SPH (smoothed particle hydrodynamics) calculations to study the stability properties of close binary NS configurations in strict hydrostatic equilibrium, and follow the evolution of unstable systems to complete coalescence. RS demonstrated for the first time that, even in Newtonian gravity, an innermost stable circular orbit (ISCO) is imposed by global hydrodynamic instabilities, which can drive a close binary system to rapid coalescence once the tidal interaction between the two NS becomes sufficiently strong. Since then many other groups have performed Newtonian calculations of binary NS coalescence, concentrating on various aspects of the problem. Most recent calculations have used either SPH (see, e.g., [10–14]), or PPM (the Eulerian, grid-based, piecewise parabolic method; see, e.g., [15–19]). Refinements have included the addition of terms to approximate energy and angular momentum losses to gravitational radiation (see [8,14,17]) and more detailed treatment of the nuclear physics (e.g. [13,18], with applications to models of gamma-ray bursts).

The first calculations to include the lowest-order post-Newtonian (1PN) corrections to Newtonian gravity, as well as the lowest-order dissipative effects of the gravitational radiation reaction (2.5PN) were performed by Oohara and Nakamura using an Eulerian grid-based method [20]. More recently, Faber and Rasio ([21], hereafter Paper 1), and Ayal et al. [22], have performed SPH calculations that included all 1PN and 2.5PN corrections, using a PN formalism developed by Blanchet, Damour, and Schäfer ([23], hereafter BDS).

These calculations revealed that the addition of 1PN corrections to the hydrodynamic equations can have a marked effect on the gravity wave signal. In Paper 1, we presented a detailed comparison between two coalescence calculations (for initially synchronized binaries containing two identical stars modeled as simple $\Gamma = 3$ polytropes), one including both 1PN and 2.5PN corrections, and the other including only Newtonian gravity plus radiation reaction (2.5PN

corrections). We found that the 1PN effects produce several luminosity peaks in the gravity wave emission, whereas the Newtonian merger shows a simpler signal with a single peak followed by exponential damping of the emission. In addition, 1PN effects accelerate the final coalescence and produce large tidal lag angles for both NS just prior to contact, leading to a more “off-center” collision. This produces a complex pattern of quadrupole oscillation and differential rotation in the merger remnant, accompanied by a characteristic modulation of the gravity wave signal.

Several groups have been working on fully general relativistic (GR) calculations of NS mergers, combining the techniques of numerical relativity and numerical hydrodynamics in 3D [24–26]. However, this work is still in the early stages of development, and only preliminary results have been reported so far. Obtaining accurate gravitational radiation wave forms from full GR simulations is particularly difficult, since the waves must be extracted at the outer boundaries of large 3D grids extending out into the true wave zone of the problem. However, fully GR calculations are essential for addressing the question of the stability to gravitational collapse and ultimate fate of a merger. Using a GR formalism developed by Shibata [25], Shibata and Uryu [26] find that collapse to a black hole on a dynamical time scale during final coalescence does not happen for NS with stiff EOS and realistic parameters. Only with unrealistically compact initial NS models (starting already very close to the maximum stable mass) does collapse to a black hole occur on the merger time scale. This confirms our expectations from the discussion in Paper 1: for realistic NS with stiff EOS, PN calculations of binary coalescence can provide results that remain at least qualitatively correct all the way to a complete merger.

In this paper, we continue the work begun in Paper 1, using our PN SPH code to study the coalescence of NS binaries. Here, we relax some of the simplifying assumptions made in Paper 1 in constructing the initial models for NS binary systems. We no longer assume the binary system to contain two identical stars, and perform several calculations for binary mass ratios $q \neq 1$. We also allow for a nonsynchronized initial configuration, instead of the rigidly rotating binary system assumed in Paper 1. Finally, we consider NS with somewhat softer EOS, but still modeled as simple polytropes. In the rest of this section, we discuss the theoretical and observational constraints on these various assumptions.

Mass measurements for NS derived from the timing of relativistic binary radio pulsars are all consistent with a remarkably narrow underlying Gaussian distribution with $M_{NS} = 1.35 \pm 0.04 M_{\odot}$ [27]. The largest observed departure from $q = 1$ in any known binary pulsar with likely NS companion is currently $q = 1.386/1.442 = 0.96$ for the Hulse-Taylor pulsar PSR B1913+16 [28]. For comparison, $q = 1.349/1.363 = 0.99$ for PSR B2127+11C [29], and $q = 1.339/1.339 = 1$ for PSR B1534+12 [27,30]. Although the equal-mass case is clearly important, one should not conclude from these observations that it is unnecessary to consider coalescing NS binaries with unequal-mass components. Indeed, it cannot be excluded that other binary NS systems (that may not be observable as binary pulsars) could contain stars with significantly different masses, especially considering the different histories of the primary and secondary in most binary NS evolution scenarios. Theoretically, the predicted NS masses from stellar evolution and supernova calculations span a considerably wider range than observed [31]. Moreover, Newtonian calculations of binary NS coalescence (RS2, [11]) have shown that even very small departures from $q = 1$ can drastically affect the hydrodynamics. A small asymmetry in the initial system grows rapidly during the merger, and there is almost no disruption of the primary (more massive star), which simply sinks to the center of the merger remnant (RS2). A more extreme asymmetry, such as $q \simeq 0.5$, can lead to a brief episode of mass transfer from the secondary (less massive star) onto the primary, followed by a sudden widening of the binary system, rather than a merger (RS2). The same behavior is seen in hydrodynamic simulations of coalescing binaries containing a NS in orbit around a more massive black hole (see [32,33]). In this paper, we will not consider such extreme mass ratios, but will focus instead on covering well a narrower but realistic range of values from $q = 0.8$ to $q = 1$ (For comparison, previous, purely Newtonian calculations have been performed for $q = 0.5$ and $q = 0.85$; see RS2, [11]).

Because of the low viscosity of the NS fluid, the tidal synchronization time for NS binaries is always considerably longer than the orbital decay time scale. Therefore, it is expected that the NS should be spinning slowly prior to final coalescence [34]. In the limit of nonspinning stars at large separation, the binary configuration just prior to final coalescence will be *irrotational*, i.e., the fluid motion inside each star will have zero vorticity, although it can have a small amount of angular momentum ([34–36]). In contrast, in many previous studies of NS binary coalescence (and in Paper 1), *synchronized* initial conditions have been used for simplicity (RS2, [7,8,15,16,20]). For a synchronized binary, the entire mass of fluid is in rigid rotation, and an equilibrium initial configuration can be constructed easily using relaxation techniques in the corotating frame of the binary (where the problem reduces to hydrostatics). These relaxed initial conditions, while somewhat unphysical, are much less susceptible to spurious oscillations of the fluid around the correct quasi-equilibrium configuration (RS). In this paper, we will present a method for constructing accurate irrotational initial conditions, and we will compare the results of PN calculations for the coalescence of irrotational NS binaries to those obtained in Paper 1 for initially synchronized NS binaries.

Here, as in Paper 1, we model NS with a stiff EOS as simple polytropes, i.e., the pressure P is a function of the density only, of the form $P = kr_{*}^{\Gamma}$, where k is called the polytropic constant, Γ is the adiabatic exponent, and r_{*} is the rest mass density of the fluid (we adopt the notation of BDS), not to be confused with the total mass-energy density

of the fluid [37].

A polytropic EOS provides a convenient approximation to many different realistic NS EOS calculated under various assumptions about the still uncertain microphysics above nuclear density. Higher values of Γ represent stiffer EOS, while lower values represent softer EOS. In addition, it allows for direct comparison to previous Newtonian work, which was done mainly for polytropes. The most commonly adopted polytropic EOS for NS uses $\Gamma = 2$ (RS1, [10,15,16]). Newtonian polytropes with $\Gamma = 2$ have a radius that is independent of mass, a well-known property satisfied approximately by all realistic NS models ([38]). Several tabulated NS EOS are found to have effective adiabatic exponents that are close to this value, or slightly higher. In particular, the Lattimer-Swesty EOS [39], used in several previous calculations [13,14,17–19] has an effective adiabatic index $\Gamma \simeq 2.3$ for a $1.4 M_\odot$ NS, assuming the lowest available value of the nuclear compressibility ($K = 180$ MeV). The latest microscopic NS EOS, constrained by nucleon scattering data and the binding of light nuclei, and incorporating three-body forces, are even stiffer, with $\Gamma \simeq 3$ (see, e.g., [40] for a summary, [41] for a recent update, and [36] for polytropic fits). In this paper, we will present and compare calculations performed for $\Gamma = 3$ (as in Paper 1), and for $\Gamma = 2$. We feel that this range corresponds reasonably to the theoretical uncertainty in recent determinations of the NS EOS. We will *not* consider in this paper the much softer EOS that may result from even more uncertain considerations of exotic states of matter such as pion condensates or strange quark matter [42]. Note that PN expansions are more difficult to do consistently with softer EOS, since the stars are more centrally condensed and thus the central gravitational field is much stronger. There is some advantage to using softer EOS within the framework of the BDS formalism, however, since smaller values of Γ help keep several 1PN quantities small (see Paper 1, Eqs. A10-12). A key difference between stiffer and softer EOS is captured by our range of adiabatic exponents. Indeed, previous Newtonian work has shown a significant difference between $\Gamma = 2$ and $\Gamma = 3$, since polytropes with $\Gamma \gtrsim 2.4$ can support a stable, rapidly rotating *triaxial* configuration, which would lead to a persistent gravity wave signal, whereas those with $\Gamma \lesssim 2.4$ generally damp out to oblate *spheroids*, which have no time-dependent quadrupole moment and therefore cannot radiate gravity waves (RS2). The existence of a long-lasting exponentially damped gravity-wave emission tail would have a significant effect on the integrated power spectrum of the gravitational radiation signal from binary coalescence.

The outline of our paper is as follows. Section II presents our numerical methods, including a brief description of our PN SPH code, and the procedure used to construct irrotational initial conditions (The construction of synchronized initial conditions and the SPH method are discussed in more details in Paper 1). Additionally, we describe the parameters and assumptions for all runs quoted in this paper. Section III presents our numerical results, focusing in turn on the effects of varying the EOS, the mass ratio, and the initial spins, as well as the differences between Newtonian runs and PN runs. Motivation for future work as well as a brief summary of our results to date are presented in Section IV.

II. NUMERICAL METHODS AND SUMMARY OF CALCULATIONS

A. The PN SPH code

All our calculations were performed using the post-Newtonian (PN) smoothed particle hydrodynamics (SPH) code described in detail in Paper 1. It is a Lagrangian, particle-based code, which has been adapted to the PN formalism of BDS. As in Paper 1, we use a hybrid 1PN/2.5PN formalism, in which 1PN corrections are artificially scaled down, so as to remain numerically tractable, while 2.5PN effects are included for realistic NS parameters. Throughout this paper we use units such that $G = M = R = 1$, where M and R are the rest mass and radius of the primary NS. In these units, there are then two different values of the speed of light c corresponding to the 1PN and 2.5PN corrections. As in Paper 1, we take $c_{2.5PN} = 2.5$, which gives $GM/Rc_{2.5PN}^2 = 0.16$, corresponding to realistic NS parameters, but we take $c_{1PN} = 4.47$, giving $GM/Rc_{1PN}^2 = 0.05$, to keep all 1PN quantities sufficiently small.

Models for the primary NS with a $\Gamma = 3$ polytropic EOS (i.e., $P = kr_s^3$) were taken from Paper 1. To construct models for the secondary NS when $q \neq 1$, we kept the same value of the polytropic constant k determined for a primary with $GM/Rc^2 = 0.05$, but we computed models with a lower mass using a relaxation technique. Note that, in contrast to their Newtonian counterparts, PN polytropes do not obey a simple power-law mass-radius relation, and therefore models for the secondary cannot be obtained simply by rescaling models for the primary. Additionally, we computed a series of $\Gamma = 2$ polytropic models for single NS with values of GM/Rc^2 between 0.01 and 0.05, as well as lower-mass models based on the primary model with $GM/Rc^2 = 0.05$. While Newtonian polytropes with $\Gamma = 2$ have a radius independent of the mass (for fixed k), the radius of a PN $\Gamma = 2$ polytrope increases with decreasing mass. The properties of the $\Gamma = 2$ PN polytropic sequence are summarized in Table I and the properties of NS models with lower masses are listed in Table II.

To set up synchronized initial conditions, we used the same relaxation scheme described in Paper 1 to create accurate equilibrium configurations. The two NS are initially placed along the x axis, with a binary separation r_0 (distance between the centers of mass of the two stars), and the binary center of mass at the origin. The orbital motion is assumed to be in the $x - y$ plane, and the orbital angular momentum vector in the positive z direction. We assume that all SPH particle velocities \mathbf{v}_i vanish in the corotating frame of the binary, and we use an iterative method to find the proper force on each particle in equilibrium, holding the binary separation fixed. As discussed in Paper 1, there are subtle differences between the particle velocities \mathbf{v}_i and momenta \mathbf{w}_i , which must be treated with care (see Paper 1, Eqs. A23–24, and Eq. B8). The angular velocity Ω of the corotating system is calculated from the centripetal accelerations of the two components of the binary,

$$\Omega = \sqrt{\frac{-\dot{v}_x^{(1)} + \dot{v}_x^{(2)}}{2r_0}}. \quad (1)$$

Here $\mathbf{v}^{(1)}$ and $\mathbf{v}^{(2)}$ are the center-of-mass velocities of the primary (located on the positive x side) and secondary (located on the negative x side), respectively. As in Paper 1, we set the initial velocity field of the fluid to be $v_x = -\Omega y$, $v_y = \Omega x$ when the dynamical run is started (in the inertial frame).

B. Irrotational initial conditions

Since there is no simple way to relax an irrotational binary configuration, to strict equilibrium, we used the results of Lombardi, Rasio, and Shapiro ([43], hereafter LRS) to construct approximate initial conditions. LRS calculated PN equilibrium solutions for irrotational binary NS with polytropic EOS, assumed to have self-similar ellipsoidal density profiles, with the density as a function of radius given by the 1PN expansion of the Lane-Emden equation. Approximate solutions were determined by minimizing the total energy of the binary configuration, including 1PN terms. The resulting NS models are the compressible, PN analogues of the classical Darwin-Riemann ellipsoids for incompressible fluids [35,44,45].

In this paper we will only consider a single irrotational binary model, with $q = 1$ and $\Gamma = 3$. To construct the initial binary model, we adopt the equilibrium shape of the stars determined by LRS, but in combination with the internal structure of our single star models (calculated previously for synchronized initial conditions). Since our PN runs were started from a rather large initial separation, $r_0 = 4.0 R$, where the tidal deformations are still extremely small, we find that the initial oscillations that result from small departures from true equilibrium are negligible. For an EOS with $\Gamma = 3$ ($n = 0.5$, where $n = 1/(\Gamma - 1)$ is the polytropic index), an initial separation of $4.0 R$, and a compactness $GM/Rc^2 = 0.05$, we find from Table III of LRS that the axes of the ellipsoidal figure for each star are given by $a_1/R \simeq 1.02$, $a_2/a_1 \simeq 0.96$, and $a_3/a_1 \simeq 0.96$. Here a_1 is along the binary axis (x -direction), a_2 is in the direction of the orbital motion (y -direction), and a_3 is along the rotation axis (z -direction).

The initial velocities of all SPH particles are calculated from Eqs. 18-20 of LRS, which give

$$v_x = -\Omega y \left(1 - \frac{2a_1^2}{a_1^2 + a_2^2}\right) \quad (2)$$

$$v_y = \Omega x \left(1 - \frac{2a_2^2}{a_1^2 + a_2^2}\right). \quad (3)$$

It is easy to verify that this initial velocity field has zero vorticity in the inertial frame. We determine the angular velocity from Eq. 1, using an iterative method, since velocity derivatives have a weak velocity dependence which makes it difficult to find a self-consistent solution directly (see Paper 1, Eqs. A17-A19 and Eq. A23). We find that three iterations yields convergence to within a fraction of a percent, and six to within one part in 10^4 .

C. Summary of calculations

We performed several large-scale SPH calculations of NS binary coalescence for the equal-mass case, and a series of shorter runs designed to study the effect of varying the mass ratio q . Table III summarizes the relevant parameters of all runs performed. Following the notation of Paper 1, we refer to all runs that included both 1PN and 2.5PN effects as “PN runs”, while those runs performed without 1PN corrections are referred to as “N runs.” Note that *both* N and PN runs included the 2.5PN gravitational radiation reaction effects. We did not perform any new completely Newtonian calculations (except for a brief test run mentioned in Sec. III A).

All runs use 5×10^4 SPH particles per NS (i.e., the total number of particles $N = 10^5$), independent of q . The number of SPH particle neighbors $N_N = 100$. Shock heating, which is normally treated via the SPH artificial viscosity, was ignored, since it plays a negligible role in binary coalescence, especially for fluids with a very stiff EOS (see Paper 1). All Poisson equations were solved on grids of size 256^3 , including the space for zero-padding, which yields the proper boundary conditions. All PN runs were done using $1/c_{1PN}^2 = 0.05$ and $c_{2.5PN} = 2.5$, as in Paper 1. Since we have an ambiguity in defining the relative time coordinate for different runs, we redefine the initial time t_0 of each run in such a way that the time of the first gravity wave luminosity peak $t_{\max}^{(1)} = 20$, as in run B1 (which starts from $t = 0$). As a result, some runs started before $t = 0$ (the starting time t_0 for each run is given in the third column of Table III).

Run A1 is identical to the N run described in Paper 1, for a binary containing two identical NS modeled as $\Gamma = 3$ polytropes. This run uses Newtonian gravity with radiation reaction (2.5PN) corrections, and started from an initial separation $r_0 = 3.1 R$. Runs A2, A3, A4, and A5 feature the same initial conditions, but have mass ratios $q = 0.95, 0.90, 0.85$, and 0.80 , respectively. Unlike A1, in which the simulation ran until a stable triaxial remnant was formed, runs A2–A5 were terminated after the completion of the first peak in the gravity wave luminosity.

Run B1 is the PN run of Paper 1, also for two identical $\Gamma = 3$ polytropes, but with 1PN and 2.5PN corrections included, and an initial separation of $r_0 = 4.0 R$. Runs B2 and B3, like their Newtonian counterparts, correspond to mass ratios $q = 0.9$ and 0.8 , respectively, and the same shorter integration time.

Run C1 is a Newtonian run (with radiation reaction effects) for two identical $\Gamma = 2$ polytropes. Since the ISCO for this softer EOS is located at smaller binary separation than for $\Gamma = 3$, (see, e.g., [43]) we start this run with $r_0 = 2.9 R$. As a test, we compared the results of this run to one with all identical parameters but with a slightly larger initial separation, $r_0 = 3.1 R$, and found no measurable differences. Run C2 has a mass ratio of $q = 0.8$ and the same EOS and initial separation. Runs D1 and D2 are the 1PN counterparts of C1 and C2, with $\Gamma = 2$, an initial separation $r_0 = 4.0 R$, and $q = 1$ and $q = 0.8$, respectively. Run C2 was terminated after the first gravity wave luminosity peak, whereas run D2 was continued until a stable remnant configuration was reached, to allow for comparison with D1.

All the previous runs started from a *synchronized* initial binary configuration, as in Paper 1. In contrast, run E1 started from an *irrotational* initial condition, with the EOS, mass ratio, and initial separation as in run B1, and including all 1PN and 2.5PN terms. It was continued until a stable remnant configuration was reached.

III. RESULTS

As in Paper 1, we begin with a brief qualitative discussion of the coalescence process, but focus here on the softer EOS with $\Gamma = 2$. In Figs. 1 and 2, we compare the evolution of the system in runs C1 and D1, respectively. Both runs are for two identical NS with a $\Gamma = 2$ EOS, but run D1 includes 1PN effects whereas run C1 does not. These plots can be directly compared to Figs. 1 and 2 of Paper 1, which show the evolution of runs A1 and B1, respectively (for two identical NS with $\Gamma = 3$). As seen in Fig. 2, a significant tidal lag angle θ_{lag} develops in the PN system just prior to final merging. Values of θ_{lag} (calculated as the angle between the binary axis and the principal axis of each component) upon first contact are given in the fourth column of Table III for all runs. Note that for binaries with mass ratios $q \neq 1$, the secondary develops a larger lag angle than the primary. This effect is much more pronounced with the addition of 1PN corrections. In all cases, the merger is accompanied by mass shedding and the formation of spiral arms, which may have a significant width. These spiral arms dissipate quickly (by $t \simeq 40$ in Figs. 1 and 2) and merge to form a halo of material around the axisymmetric, oblate remnant at the center of the system. It should be noted that when we speak of “mass shedding” in this work (both Paper 1 and here), we mean that matter is ejected from the central dense core into an outer halo, but *not to infinity*. By the end of our simulations, all the matter forming the outer halo is still gravitationally bound to the system.

A. Dependence on the NS EOS

As already pointed out in Paper 1, our PN calculations of NS binary coalescence are most relevant for stiff NS EOS, for which most recent calculations give values of $GM/Rc^2 \simeq 0.1 - 0.2$ (for $M \simeq 1.5 M_\odot$). Even if the true NS EOS were much softer, making strong GR effects dominant throughout the final binary coalescence, performing hydrodynamic calculations in the PN limit would still remain important, since the PN results provide a crucial benchmark against which future full-GR calculations can be tested.

Gravitational radiation wave forms and luminosities for runs A1, B1, C1, D1 are shown in Figs. 3 and 4. The two polarizations of gravity waves are calculated for an observer at a distance d along the rotation axis of the system, in the quadrupole approximation (see Paper 1, Eqs. 23-25).

As was found for NS with a $\Gamma = 3$ EOS (Paper 1), for NS with a $\Gamma = 2$ EOS PN corrections serve to lower the maximum gravity wave luminosity. However, regardless of whether we include 1PN terms, the peak gravity wave luminosity is larger for the softer EOS.

Comparing the N and PN runs in Fig. 4, we see that, besides differences in the maximum luminosity, there are qualitative differences in the shape of the first luminosity peak. Both PN runs show asymmetry around the peak, with a long rise from $t \simeq 10 - 20$ containing a flatter section at $t \simeq 15 - 20$, and then a smooth decrease from $t \simeq 20 - 25$. This effect can be attributed to a period of slower binary infall as the two stellar cores first come into contact (as seen in Fig. 5, which shows the binary separation r as a function of time). We see that the effect is more pronounced for the PN run with a $\Gamma = 2$ EOS (D1), which has a significant drop in the inspiral rate from $t \simeq 14 - 18$, corresponding exactly with a similar plateau in the gravity wave luminosity. The effect is weaker for the PN run with the $\Gamma = 3$ EOS (B1), which displays a more symmetric gravity wave luminosity peak.

Similar behavior is seen in the N runs. For the run with a $\Gamma = 3$ EOS (A1), we see a decrease in the inspiral rate from $t = 20 - 25$, which occurs after the period of maximum gravity wave luminosity, and a simultaneous plateau in the luminosity immediately after the peak. For the $\Gamma = 2$ case (C1), we see no apparent decrease in the inspiral rate, either before or after $t = 20$. Correspondingly, this was the only run under discussion which showed an almost completely symmetric luminosity peak with respect to time.

In Fig. 6, we show the energy loss to gravitational radiation, calculated as the integral of gravity wave luminosity over time. We see that the Newtonian runs, A1 and C1, have higher energy losses, in line with the respective peak gravity wave luminosities. The secondary peaks in the $\Gamma = 3$ PN run (B1), discussed extensively in Paper 1, give a higher net energy loss than in the $\Gamma = 2$ PN run (D1), where more energy is lost during the first peak (by a significant fraction). Note that energy losses are measured from the initial point of each run. Thus, runs which had negative time offsets have $E_{GW} > 0$ at $t = 0$.

More surprisingly, perhaps, we note that a second luminosity peak is visible not only in the $\Gamma = 2$ PN run (D1), but also in run C1, for a $\Gamma = 2$ Newtonian coalescence. In Paper 1, it was shown that the gravity wave luminosity is extremely well correlated with the ratio of the first and second principal moments of inertia, I_1 and I_2 , in effect giving a measure of the ellipticity of the remnant in the orbital plane. A similar analysis is shown in Fig. 7, which compares runs C1 and D1. Note that we have used a higher density cut for this plot than was used for the $\Gamma = 3$ remnants in Paper 1. Here only, we define the inner remnant to consist of all SPH particles with local densities $r_* > 0.04$. We see again a strong correlation between ellipticity and gravity wave luminosity. In run D1, the small-amplitude oscillations with period $T \simeq 5$ are caused by an interaction with the outer material of the remnant. If we lower our density cut to include all SPH particles with local densities $r_* > 0.005$ (as in Paper 1), thereby including more of the tenuous material outside of the core of the remnant, the moment of inertia ratio shows only this oscillation, which damps out over time. Since this material contributes only weakly to the quadrupole moment, we conclude that it is the dynamics inside the core that controls the gravity wave signal.

Comparing the results of our run C1, which includes the effects of radiation reaction, with the completely Newtonian $\Gamma = 2$ run shown in RS2, we conclude that the asymmetry induced by the larger tidal lag angle is responsible for the existence of a second gravity wave luminosity peak, even for systems that eventually reach oblate, non-radiating configurations. To confirm this, we checked our results against a completely Newtonian $\Gamma = 2$ test run (without radiation reaction terms, and starting from $r_0 = 2.7$), and found that a second peak is indeed absent in this case (in agreement with RS2).

Careful inspection of Fig. 7 of Paper 1 (where run A1 is referred to as the N run), reveals very small irregularities in the otherwise smooth gravity wave luminosity at $t \simeq 33$ and 48, which correspond to the secondary gravity wave luminosity peaks found in run B1. Clearly, the existence of secondary luminosity peaks seems to be reasonably universal in these simulations. For run A1, however, modulation of the moment of inertia ratio is virtually absent, so that the effect is extremely small in this case.

B. Dependence on the binary mass ratio

The dependence of the peak amplitude $h_{\max} \equiv (h_+^2 + h_\times^2)^{1/2}_{\max}$ of gravitational waves on the mass ratio q appears to be very strong. In RS2, an approximate power law $h_{\max} \propto q^2$ was derived for nearly equal-mass systems, on the basis of two purely Newtonian calculations for $q = 1$ and $q = 0.85$. This is considerably steeper than the naïve scaling obtained for two point masses in a Keplerian orbit, which gives $h_{\max} \propto q$. Such a linear scaling is obeyed (only approximately, because of finite-size effects) by the wave amplitudes of the various systems *prior* to final coalescence. For determining the maximum amplitude during the merger, however, hydrodynamics must be taken into account. In a system with $q \neq 1$, the more massive star tends to play a far less active role in the hydrodynamics and, as a result, there is a rapid suppression of the radiation efficiency as q departs even slightly from unity. For the peak luminosity

of gravitational radiation RS found approximately $L_{\text{max}} \propto q^6$. Again, this is a much steeper dependence than one would expect based on a simple point-mass estimate, which gives $L \propto q^2(1+q)$. The results of RS were all for initially synchronized binaries, but very similar results have been obtained by Zhuge et al. [11] for binaries containing initially nonspinning stars with unequal masses.

The role of the primary and secondary is shown qualitatively in Figs. 8 and 9 for run D2, which uses a $\Gamma = 2$ EOS with $q = 0.8$, and included 1PN terms. The panels on the left show the primary, center panels the secondary, and those on the right the combined system. We see that the evolution is markedly different from that of the $q = 1$ binary shown in Fig. 2. Here, there is a single spiral arm, which is formed from the secondary as it gets tidally disrupted. Shortly after first contact is made, a stream of matter flows from the secondary toward the primary, landing on the trailing side (orbital rotation is counterclockwise), as a result of the orbital motion and the significant tidal lags present in the system upon contact. As the coalescence proceeds, the secondary is tidally stretched, with the outer portion spun out of the system while the inner part is accreted by the primary. Throughout this evolution, the primary remains relatively undisturbed, except for a small layer near its surface. By $t \simeq 40$, mass shedding is triggered and the system develops a single spiral arm, composed entirely of matter from the secondary as it is completely disrupted. Note that this single spiral arm is even wider than those seen in the $q = 1$ coalescence (with a width comparable to the initial NS radius). There is also an extremely small amount of mass shedding from the outer edge of the primary, where it joins with a high-velocity stream of matter from the secondary, on the side opposite the single spiral arm. Finally, by $t \simeq 50$, what was once the core of the secondary has fallen onto the primary, and the spiral arm has begun to dissipate, forming a low-mass halo around the system.

In Figs. 10 and 11, we show the gravitational radiation wave forms and luminosity for all but two of the synchronized binary simulations. For clarity, we only show results for runs A1, A3, and A5 in the $\Gamma = 3$ N plot, since the other runs can be safely interpolated from those present. We note that for the $\Gamma = 3$ EOS, the morphology of the peaks seen in Fig. 4 seems to be present for all mass ratios. We find plateaus in the gravity wave luminosity before the peak for PN runs, and after the peak for N runs. This behavior is much harder to see in the $\Gamma = 2$ runs with $q=0.8$, which have lower peak luminosities in general than their $\Gamma = 3$ counterparts.

In Fig. 12 we show the maximum gravity wave strain and luminosity for $\Gamma = 3$ and $\Gamma = 2$ EOS binaries, plotted as a function of the mass ratio. We find in all cases that the power-law dependence is steeper than would be predicted by the point-mass approximation. For the gravity wave strain, we see a slightly steeper power law for N runs than for PN runs. For $q = 1$, N runs have a higher peak strain, but, for both EOS, the $q = 0.8$ binaries show a higher peak strain in the PN case than in the N case. We conclude that the strictly Newtonian scaling obtained by RS2, $h_{\text{max}} \propto q^2$, remains approximately valid for Newtonian binaries with radiation reaction effects, but is almost certainly steeper than the dependence that will be present in realistic NS binaries (based on our results including 1PN effects).

For the peak gravity wave luminosity, we see a much stronger dependence on the EOS. For the softer, $\Gamma = 2$ EOS, we see that the strictly Newtonian RS2 fit of $L_{\text{max}} \propto q^6$ (obtained for $\Gamma = 3$ polytropes!) is not nearly as steep as the correct relation. Additionally, the difference between N and PN runs in magnitude is less pronounced than for the $\Gamma = 3$ EOS, where we have a $\sim 20\%$ difference rather independent of the mass ratio. For $\Gamma = 3$, we see that the RS2 fit is slightly too steep, although the correct power law remains steeper than the point-mass approximation.

C. Irrotational initial condition

To study the effects of the initial spins on the evolution of the merger we compare our run E1, with the irrotational initial condition described in Section IIB, with run B1, the PN run described extensively in Paper 1, which started from a synchronized initial condition. Particle plots for run E1 are shown in Fig. 13. Comparing to Fig. 2 of Paper 1, we see that in both cases, the stars develop a large tidal lag immediately before merger, leading to an “off-center” collision and a highly asymmetrical merger until $t \simeq 50$. A major difference, however, is the absence of mass shedding as the irrotational NS first make contact before $t = 20$. We see a very small amount of mass shedding and thin spiral arm formation from $t \simeq 25 - 35$, involving a very small fraction of the mass that was deposited into the outer halo for the synchronized case. Note that mixing of the fluids originating from the two different stars does not occur immediately after contact. Instead, as the two NS surfaces come into contact with opposite tangential velocities (in the corotating frame), a long vortex sheet forms at the interface between the two fluids (around $t \simeq 20$). This vortex sheet is Kelvin-Helmholtz unstable and breaks into a turbulent layer that can then gradually mix the fluids [46]. Unfortunately, the spurious shear viscosity inherent in any discretized simulation is much larger than the true viscosity of the NS fluids, and therefore the evolution in the turbulent region is very likely to be dominated by resolution-dependent numerical effects.

Noting that the orbital rotation for the binary is counter-clockwise, we see that all mass shedding into the spiral arms actually occurs from the leading edge of each star. Particles that were initially located at small radius relative

to the center of mass of the system travel along the vortex sheet between the two stars before being spun off. This is in direct contrast to the synchronized case, in which mass shedding occurs almost entirely from regions that are initially at large radius, on the outside of each star. Material there is ejected from the merging binary system as it spins up and overflows its effective potential well through the outer Lagrange points. Here we find no mass shedding via this mechanism, in agreement with previous work on irrotational systems [17].

In Figs. 14 and 15 we show density contours during the merger of run E1, with the velocity field of the fluid in the inertial frame overlaid. Mass shedding and spiral arm formation starts at $t \simeq 22$. In Figs. 16 and 17 we show the density and velocity field of the inner regions of the merger, with the velocities shown with respect to the mean corotating frame of the entire system. Specifically, we define the mean corotating angular velocity Ω_c by taking a weighted average over the tangential velocities of all SPH particles,

$$\Omega_c \equiv \frac{\sum_i m_i [(xv_y - yv_x)/r_{\text{cyl}}]_i}{\sum_i m_i (r_{\text{cyl}})_i}, \quad (4)$$

where the cylindrical radius is defined as $r_{\text{cyl}} \equiv (x^2 + y^2)^{1/2}$. It is easy to see that this definition reduces to the correct orbital angular velocity of the initial binary system, and to the correct angular velocity of any single, rigidly rotating object. We see that the vortex sheet formed during the merger lasts from the point of first contact at $t \simeq 15$ until $t \simeq 22$. As the coalescence proceeds, turbulence develops along the sheet, with vortices appearing immediately at the very center of the remnant, then at several points further out. We note that the central vortex is initially spinning in the direction of the orbital motion, as the initial misalignment causes matter to fall in around the center. The outer vortices are concentrated around regions of higher density, when matter from deeper inside each NS continues to fall onto the vortex sheet. From $t \simeq 22$ to $t \simeq 25$, a slightly different pattern emerges. As the core regions of the original NS continue to approach each other, the velocity field between the cores remains turbulent, but a coherent velocity field develops around the cores. Counterspinning material located toward the outer parts of the remnant connects and forms a simple pattern of circulation. Here the angular velocity appears to become negative as we move away from the center (in the inertial frame, this represents the angular velocity decreasing with increasing distance from the rotation axis). Material in the center, still somewhat turbulent but retaining the original corotating pattern, has much less angular momentum, leading to a pattern of strongly differential rotation throughout the merger remnant (See Sec. III D).

The evolution of the mean corotating angular velocity is shown in Fig. 18. It rises monotonically during the initial coalescence until $t \simeq 25$, when the inner NS cores merge. Later it fluctuates with a small amplitude around a nearly constant maximum value $\Omega_c \simeq 0.6 \simeq 1.4 \times 10^4 \text{ rad s}^{-1} (M/1.5 M_\odot)^{1/2} (R/10 \text{ km})^{-3/2}$ as the remnant contracts and relaxes. By $t \simeq 50$ it settles down with a slowly and steadily decreasing trend as the final triaxial configuration continues to lose angular momentum to gravitational radiation.

The gravitational radiation wave form for run E1 is shown in Fig. 19. There are no major qualitative differences with the wave form obtained for run B1, which has the same EOS and mass ratio, but a synchronized initial condition (see Fig. 3). The gravity wave luminosity is shown in Fig. 20, along with that of run B1. We see that irrotational initial conditions lead to a slight reduction in the maximum gravity wave luminosity, simply because the system has a smaller total angular momentum. The small-amplitude oscillations in the luminosity of run E1 for $t \simeq 0 - 15$ result from small deviations from quasi-equilibrium in the initial binary of magnitude $\delta\rho_c/\rho_c \simeq 0.05$. This small amplitude gives us confidence that the use of self-similar PN ellipsoids in the construction of our irrotational initial condition represents a very small source of error for these calculations. Our irrotational ellipsoids, although still approximate, are considerably better than the spherical models used in all previous studies (see, e.g., [11,17]).

Both the E1 and B1 runs show a significant second luminosity peak in the gravity wave emission, although the magnitude of the second peak is again smaller for the irrotational case. This second peak occurs at $t \simeq 33$ for both runs, indicating that the period between peaks in the gravity wave signal seems to depend primarily on the NS EOS and not on the initial spins. Note also in Table III that the second peaks for runs with a $\Gamma = 2$ EOS are at different times, whereas for $\Gamma = 3$, the peaks are always coincident. A third peak is also visible for the irrotational run, but it is of much lower amplitude, indicating that the final remnant is more nearly axisymmetric.

D. Structure of the final merger remnants

It was found in Paper 1 that the addition of 1PN corrections to the hydrodynamics has the effect of reducing mass shedding for mergers of NS with a $\Gamma = 3$ EOS. In Fig. 21, we show the evolution of the remnant mass M_r for runs C1 and D1, and find the same behavior for a $\Gamma = 2$ EOS. We show two different density cuts to highlight this behavior. By taking all SPH particles with a local density $r_* > 0.005$, we extend our definition of the “remnant” far into the outer halo. Instead, a density cut of $r_* > 0.04$ includes just the inner part of the remnant, and excludes any material

that was ejected into spiral arms. In both runs mass shedding starts occurring approximately at the time of maximum gravity wave emission ($t = 20$), and lasts for a total time $\delta t \simeq 10$, but in the PN case the mass shedding rate is significantly smaller, leading to approximately half the total amount of mass shedding as in the Newtonian case.

In Fig. 22, we show the radial mass profiles of the inner remnants for the four synchronized $q = 1$ runs. We see that the mass profile at small radii is primarily determined by the EOS, with the $\Gamma = 2$ models showing slightly more central concentration, as would be expected, although the inclusion of 1PN effects does decrease the enclosed mass in a given cylinder. At $r_{\text{cyl}} \simeq 1.2$, however, we start to see significant differences between runs with and without 1PN corrections. In the Newtonian runs, matter is ejected much more efficiently to large radii, and thus the final mass of the inner remnant falls in the range $M_r = 1.7 - 1.8$, whereas for the PN runs it is $M_r \simeq 1.9$. The remaining mass, ejected through the spiral arms, forms the halo around the inner remnant. Here we can see from the slopes of the mass profiles near $r_{\text{cyl}} \simeq 2$ that for a softer ($\Gamma = 2$) EOS, the density in the halo near the inner remnant is still significant, indicating more mass in the inner region of the halo. This is not a surprise since, as already noted by RS2, a softer EOS produces wider spiral arms, which in turn dissipate more quickly and transport material less efficiently out to very large radii.

In Table III, we list in the last three columns the total rest mass M_r , gravitating mass M_{gr} , and Kerr parameter a_r of the inner remnant at $t = 60$. Here the inner remnant includes all SPH particles out to a radius $r = 2$ (The results are rather insensitive to the precise choice of density cut, since the material in the halo is very tenuous). As was done in Paper 1, the Kerr parameter for all PN runs is taken to be $a_r = cJ_r/M_{gr}^2$, where J_r is the 1PN angular momentum of the remnant.

A comparison of the angular velocity profiles of the remnants is shown in Fig. 23. We see, quite surprisingly, that the $\Gamma = 3$ run without 1PN corrections (A1) leads to a different form than each of the other runs. All are differentially rotating, but in all other cases the angular velocity drops as a function of distance away from the rotation axis, whereas in run A1 it increases monotonically out to $r_{\text{cyl}} \simeq 1.4$, which is close to the surface of the inner remnant. Only run A1 agrees with previous purely Newtonian calculations (RS1, RS2), which found that the angular velocity increases with increasing distance from the rotation axis. However, in agreement with all previous studies, we find that the rotation profiles of all our merger remnants are pseudo-barotropic, i.e., Ω is a constant on cylinders. Recent fully GR calculations have indicated that differential rotation can increase very significantly the maximum stable mass of neutron stars [47], which makes it more likely that merger remnants can be dynamically stable against collapse to a black hole. However, differentially rotating configurations could still be secularly unstable on a viscous timescale.

Run A1 is the only one that did not produce a second gravity wave luminosity peak, suggesting that perhaps the combination of Newtonian gravity and the stiffer EOS can lead to a lower central angular momentum. In turn, this could suppress the quadrupole oscillations shown in Fig. 7. We also note a general difference in rotational velocity between the PN runs and the Newtonian runs, with both N runs showing an increase in angular velocity near the surface of the inner remnant, from $r_{\text{cyl}} \simeq 1.2 - 1.4$, whereas the PN runs show a steady decrease through this range and out into the halo.

The final structure of the merger remnant appears remarkably independent of the initial NS spins. In Fig. 24 we show the mass and angular velocity profiles of the merger remnant for the irrotational binary of run E1, compared with that of the synchronized system in run B1. We see that the two merger remnants have very similar profiles. Both remnants are differentially rotating with an angular velocity that decreases with increasing distance from the axis. The irrotational binary merger remnant has a slightly smaller angular velocity at large radii and a slightly less centrally concentrated mass profile. Note also that at large radii, the mass of the remnant for the irrotational case is essentially $M_r = 2$, i.e., very little mass shedding occurred.

IV. SUMMARY AND DIRECTIONS FOR FUTURE WORK

Using the Lagrangian SPH code described in Paper 1, which is complete to 1PN order and also includes all 2.5PN radiation reaction effects, we have further investigated the properties of NS binary mergers in PN gravity. In addition to the method presented in Paper 1 for constructing PN equilibrium initial conditions for synchronized binaries, we have used the results of the analytic work by LRS based on compressible ellipsoids to create realistic irrotational initial conditions. Our approach takes an exact, spherical PN equilibrium model computed for an isolated NS, and deforms it according to the shape of the irrotational Darwin-Riemann ellipsoid solution determined from the energy variational method of LRS.

Using the hybrid formalism of Paper 1, in which radiation reaction is treated realistically but 1PN effects are scaled down in amplitude to remain numerically tractable, we have studied the effect of PN corrections on several aspects of binary NS mergers. We find that NS with a softer EOS, modeled here as $\Gamma = 2$ polytropes, produce higher gravity wave luminosities during the merger than NS with stiffer EOS (modeled here and in Paper 1 as $\Gamma = 3$ polytropes).

As was found in previous, purely Newtonian calculations, the final merger remnant produced when $\Gamma = 2$ is an oblate spheroid, rather than a triaxial ellipsoid (obtained for $\Gamma = 3$). For calculations with and without 1PN effects, we find a strong second peak of gravity wave luminosity for a $\Gamma = 2$ EOS, in contrast to the result obtained in Paper 1, where we found that for a $\Gamma = 3$ EOS, a strong second peak of emission is present only when 1PN effects are included.

By holding the EOS and the primary NS mass fixed while varying the secondary NS mass, we have studied the dependence of the gravity wave emission on the binary mass ratio. We find that the steep power-law scaling $h_{\max} \propto q^2$ for the maximum amplitude, derived from purely Newtonian calculations in RS2 for a $\Gamma = 2$ EOS, remains approximately correct in PN gravity, for both $\Gamma = 2$ and $\Gamma = 3$ EOS. In both cases the dependence on q appears slightly steeper when 1PN effects are neglected (but while retaining 2.5PN effects). The maximum gravity wave luminosity for PN mergers follows a slightly steeper power law than the $L_{\max} \propto q^6$ found by RS2 for the $\Gamma = 2$ EOS, but is significantly flatter for the $\Gamma = 3$ EOS.

Our coalescence calculation using an irrotational initial condition shows clearly the development of a vortex sheet along the surface of contact. A turbulent region is seen until the time when the inner cores of the two NS begin to merge, at which point a stable, differentially rotating configuration is created. While the main gravity wave luminosity peak is smaller than for a synchronized initial condition, the second peak is of similar relative amplitude and coincident in time. A strong third peak was not observed for the irrotational case. The density and rotation profiles of the inner remnant appear remarkably independent of the degree of synchronization of the initial binary.

We find that, in general, the addition of 1PN effects decreases the mass in the outer halo of the merger remnant, especially when an irrotational initial condition is used. For this latter case, almost no mass at all is ejected through spiral arms during the merger. Since the 1PN corrections are artificially reduced in our calculations, we expect that for two NS with realistic parameters and an irrotational initial configuration, no matter at all will be ejected. When a synchronized initial condition is used, we find that the halo around the remnant is much denser and less extended for a softer NS EOS.

Our results have potentially important consequences for theoretical models of GRBs based on NS binary mergers [18,48]. Although current models for *long* bursts and their associated observed afterglows favor an origin in massive star collapse, NS mergers remain an attractive source at least for the separate class of *short* bursts [49]. Currently the most popular models all assume that a binary NS merger leads to the formation of a rapidly rotating Kerr BH surrounded by a torus of ejected material. Energy can then be extracted either from the rotation of the BH or from the material in the torus so that, with sufficient beaming, the gamma-ray fluxes observed from even the most distant GRBs can be explained [50]. However, our results suggest that the merger of two $1.4 M_{\odot}$ NS with stiff EOS forms an object that will *not* collapse to a BH on a dynamical time (see Paper I, Sec. IIID), in agreement with the preliminary full GR calculations of Shibata and Uryu [26]. Moreover, for irrotational binaries (containing two slowly spinning NS; see Sec. IIIC), we predict that *no matter* will be ejected during the merger, implying that no outer torus will form around the central core (see Sec. IIID). Even if the central core were to collapse to form a Kerr BH (which is not prevented by rotation, since $a_r < 1$; see Table III), energy could not be extracted to power a GRB.

Our future work using PN SPH will focus on the more realistic irrotational initial conditions introduced in this paper, while again varying the other parameters of the problem such as the binary mass ratio and the NS EOS. We will also study the dependence of our numerical results on the spatial resolution of the calculations by systematically varying the number of SPH particles from $N \sim 10^4$ all the way to $N \sim 10^6$ (which will take full advantage of our highly optimized parallel SPH code). We will try to establish that our conclusions about the gravity wave signal and final merger remnant configuration are free from numerical artifacts, in spite of the difficulties described in Sec. IIIC. Increased resolution should also yield a better understanding of the nature of the vortex sheet formed upon first contact of the binary components, and of the details of the transition to a differentially rotating configuration. We also plan to study the properties of the gravitational wave signals in Fourier space (as was done for the first time by Zhuge *et al.* [10,11] based on their Newtonian SPH calculations), since the spectral information is crucial to the interpretation of future results from LIGO and similar instruments. We will study systematically the dependence of the power spectrum of the gravitational radiation on the binary mass ratio, and on the NS EOS, as well as investigate the effects of 1PN corrections on the power spectrum.

ACKNOWLEDGMENTS

This work was supported in part by NSF Grants AST-9618116 and PHY-0070918 and NASA ATP Grant NAG5-8460. F.A.R. was supported in part by an Alfred P. Sloan Research Fellowship. The computations were supported by the National Computational Science Alliance under grant AST980014N and utilized the NCSA SGI/CRAY Origin2000.

-
- [1] A. Abramovici *et al.*, Science **256**, 325 (1992); A. Abramovici *et al.*, Phys. Lett. A **218**, 157 (1996).
 - [2] C. Bradaschia *et al.*, Nucl. Instrum. Methods **A289**, 518 (1990); B. Caron *et al.*, Class. Quantum Grav. **14**, 1461 (1997).
 - [3] J. Hough, in *Proceedings of the Sixth Marcel Grossmann Meeting*, edited by H. Sato and T. Nakamura (World Scientific, Singapore, 1992), p. 192.
 - [4] K. Danzmann, in *Relativistic Astrophysics*, proceedings of the 162nd W.E. Heraeus Seminar, edited by H. Riffert *et al.* (Wiesbaden: Vieweg Verlag, 1998), p.48.
 - [5] K. Kuroda *et al.*, in *Proceedings of the International Conference on Gravitational Waves: Sources and Detectors*, edited by I. Ciufolini and F. Fidecard (World Scientific, 1997), p.100.
 - [6] B.J. Meers, Phys. Rev. D **38**, 2317 (1988); K.A. Strain and B.J. Meers, Phys. Rev. Lett. **66**, 1391 (1991).
 - [7] K. Oohara and T. Nakamura, Prog. Theor. Phys. **82**, 535 (1989); T. Nakamura and K. Oohara, *ibid.* **82**, 1066 (1989); K. Oohara and T. Nakamura, *ibid.* **83**, 906 (1990); T. Nakamura and K. Oohara, *ibid.* **86**, 73 (1991).
 - [8] M. Shibata, K. Oohara, and T. Nakamura, Prog. Theor. Phys. **88**, 1079 (1992); **89**, 809 (1993).
 - [9] F.A. Rasio and S.L. Shapiro, Astrophys. J. **401**, 226 (1992) [RS1]; **432**, 242 (1994) [RS2]; **438**, 887 (1995) [RS3].
 - [10] X. Zhuge, J. Centrella, and S. McMillan, Phys. Rev. D **50**, 6247 (1994).
 - [11] X. Zhuge, J. Centrella, and S. McMillan, Phys. Rev. D **54**, 7261 (1996).
 - [12] M.B. Davies, W. Benz, T. Piran, and F.K. Thielemann, Astrophys. J. **431**, 742 (1994)
 - [13] S. Rosswog *et al.*, Astron. Astrophys. **341**, 499 (1999).
 - [14] S. Rosswog, M.B. Davies, F.-K. Thielemann, and T. Piran, Astron. Astrophys. **360**, 171 (2000).
 - [15] K.C.B. New and J.E. Tohline, Astrophys. J. **490**, 311 (1997).
 - [16] F.D. Swesty, E.Y.M. Wang, and A.C. Calder, Astrophys. J. (to be published), astro-ph/9911192.
 - [17] M. Ruffert, H.-Th. Janka, and G. Schäfer, Astron. Astrophys. **311**, 532 (1996).
 - [18] M. Ruffert, H.-Th. Janka, K. Takahashi, and G. Schäfer, Astron. Astrophys. **319**, 122 (1997).
 - [19] M. Ruffert, M. Rampp, and H.-Th. Janka, Astron. Astrophys. **321**, 991 (1997).
 - [20] K. Oohara and T. Nakamura, Prog. Theor. Phys. **88**, 307 (1992).
 - [21] J.A. Faber and F.A. Rasio, Phys. Rev. D, **62**, 064012 (2000) [Paper 1].
 - [22] S. Ayal *et al.*, Astrophys. J. (submitted), astro-ph/9910154.
 - [23] L. Blanchet, T. Damour, and G. Schäfer, Mon. Not. R. Astron. Soc. **242**, 289 (1990) [BDS].
 - [24] T.W. Baumgarte, S.A. Hughes, and S.L. Shapiro, Phys. Rev. D **60**, 087501 (1999); W. Landry and S.A. Teukolsky, Phys. Rev. D (to be published), gr-qc/9912004; M. Miller, W. Suen, and M. Tobias, Phys. Rev. D (to be published), gr-qc/9910022; E. Seidel, in *Relativistic Astrophysics*, proceedings of the 162nd W.E. Heraeus Seminar, edited by H. Riffert *et al.* (Wiesbaden: Vieweg Verlag, 1998), p.229.
 - [25] M. Shibata, Phys. Rev. D **60**, 104052 (1999).
 - [26] M. Shibata and K. Uryu, Phys. Rev. D. **61**, 064001 (2000).
 - [27] S.E. Thorsett and D. Chakrabarty, D. Astrophys. J. **512**, 288 (1999).
 - [28] J.H. Taylor and J.M. Weisberg, Astrophys. J. **345**, 434 (1989).
 - [29] W.T.S. Deich and S.R. Kulkarni, in *IAU Symp. 165: Compact Stars in Binaries*, edited by J. van Paradijs, E.P.J. van den Heuvel, and E. Kuulkers (Kluwer Academic Publishers, Dordrecht, 1995).
 - [30] A. Wolszczan, Nature **350**, 688 (1991).
 - [31] F.X. Timmes, S.E. Woosley, and T.A. Weaver, Astrophys. J. **457**, 834 (1996); V. Kalogera, and C.L. Fryer, Astrophys. J. (submitted), astro-ph/9911312.
 - [32] H.-Th. Janka, Th. Eberl, M. Ruffert, and C.L. Fryer, Astrophys. J. Lett. **527**, L39 (1999).
 - [33] W.H. Lee and W.L. Kluzniak, Astrophys. J. **526**, 178 (1999); Mon. Not. R. Astron. Soc. **308**, 780 (1999).
 - [34] C.S. Kochanek, Astrophys. J. **398**, 234 (1992); L. Bildsten and C. Cutler, *ibid.* **400**, 175 (1992).
 - [35] D. Lai, F.A. Rasio, and S.L. Shapiro, Astrophys. J. Lett. **406**, L63 (1993).
 - [36] D. Lai, F.A. Rasio, and S.L. Shapiro, Astrophys. J. **420**, 811 (1994).
 - [37] Note that BDS use r to denote the mass-energy density, while we use r in this paper (and in Paper 1) to denote the radial distance from the origin of our coordinate system. The two BDS quantities r and r_* become equal in the Newtonian limit, but differ at the 1PN level. Similarly, M , the total baryonic mass defined in terms of r_* , will differ by 1PN terms from M_g , the total gravitating mass. See Eqs. 3 and 4 of Paper 1 for a more detailed discussion.
 - [38] S.L. Shapiro and S. Teukolsky, *Black Holes, White Dwarfs, and Neutron Stars* (Wiley, New York, 1983).
 - [39] J.M. Lattimer and D. Swesty, Nucl. Phys. **A535**, 331 (1991).
 - [40] G. Baym, in *Neutron Stars: Theory and Observation*, edited by J. Ventura and D. Pines (Dordrecht, Kluwer, 1991), p. 21.
 - [41] A. Akmal, V.R. Pandharipande, and D.G. Ravenhall, Phys. Rev. C **58**, 1804 (1998).
 - [42] N.K. Glendenning, Phys. Rev. D **46**, 1274 (1992); G.E. Brown and H.A. Bethe, Astrophys. J. **423**, 659 (1994).
 - [43] J.C. Lombardi, F.A. Rasio, and S.L. Shapiro, Phys. Rev. D **56**, 3416 (1997) [LRS].

- [44] S. Chandrasekhar, *Ellipsoidal Figures of Equilibrium; Revised Dover Edition* (Yale University Press, New Haven, 1987).
- [45] Note that, recently, many other groups have obtained approximate solutions for irrotational close binary configurations containing polytropes, both in Newtonian and PN gravity, and in full GR. See K. Taniguchi and T. Nakamura, Phys. Rev. D (to be published), astro-ph/0004010; Phys. Rev. Lett. **84**, 581 (2000); K. Uryu and Y. Eriguchi, Phys. Rev. D **61**, 124023 (2000); S. Bonazzola, E. Gourgoulhon, and J.-A. Marck, Phys. Rev. Lett. **82** 892, (1999); K. Taniguchi, Prog. Theor. Phys. **101**, 283 (1999); S.A. Teukolsky, Astrophys. J. **504**, 402 (1998).
- [46] F.A. Rasio and S.L. Shapiro, in *IAU Symp. 165: Compact Stars in Binaries*, edited by J. van Paradijs, E.P.J. van den Heuvel, and E. Kuulkers (Kluwer Academic Publishers, Dordrecht, 1995); F.A. Rasio and S.L. Shapiro, Class. Quantum Grav. **16**, 1 (1999).
- [47] T.W. Baumgarte, S.L. Shapiro, and M. Shibata, Astrophys. J. Lett. **528**, L29 (2000).
- [48] D. Eichler, M. Livio, T. Piran, and D.N. Schramm, Nature **340**, 126 (1989); R. Narayan, B. Paczyński, and T. Piran, Astrophys. J. Lett. **395**, L83 (1992); P. Meszaros and M.J. Rees, Astrophys. J. **397**, 570 (1992); V.M. Lipunov *et al.*, *ibid.* **454**, 593 (1995); J.S. Bloom, S. Sigurdsson, and O.R. Pols, Mon. Not. R. Astron. Soc. **305**, 763 (1999).
- [49] C. Kouveliotou *et al.*, Astrophys. J. Lett. **413**, L101 (1993); A.I. MacFayden and S.E. Woosley, Astrophys. J. **524**, 262 (1999); P. Meszaros, Nucl. Phys. Proc. Suppl. **80**, 63 (2000); M. Livio and E. Waxman, Astrophys. J. **538**, 187 (2000).
- [50] P. Meszaros, M.J. Rees, and R.A.M.J. Wijers, New Astron. **4**, 303 (1999).

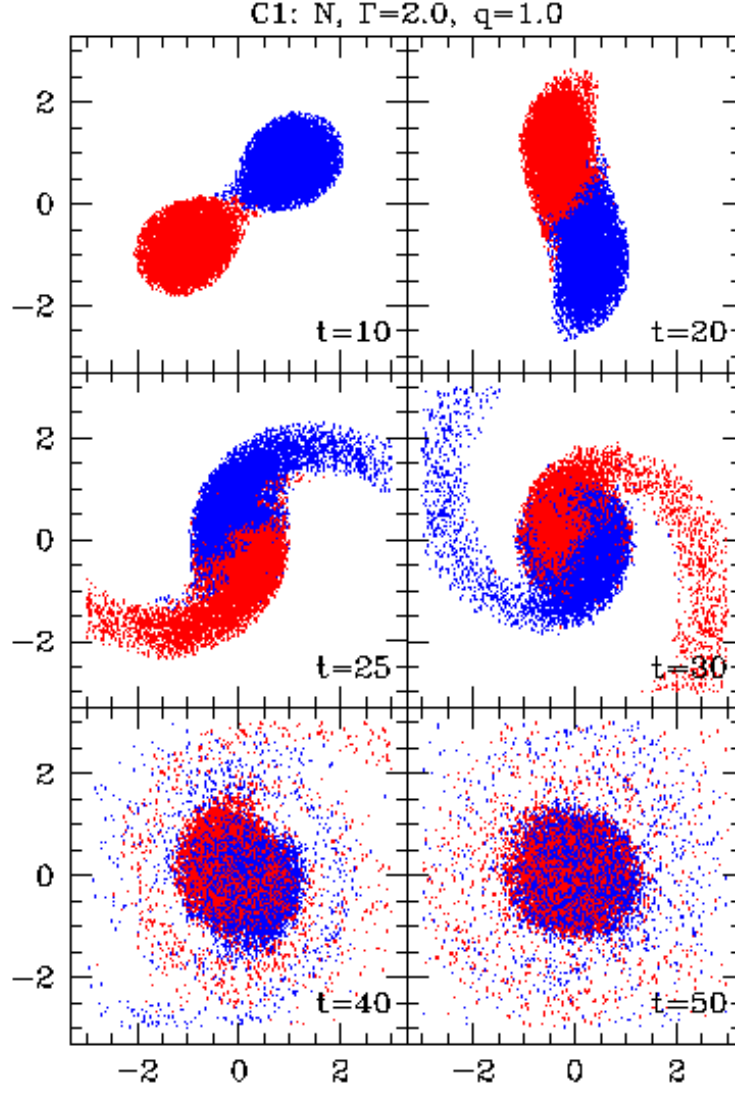


FIG. 1. Evolution of the system for Run C1 with $\Gamma = 2$ and $q = 1$. This run includes Newtonian gravity and radiation reaction (2.5PN) corrections. Projections of a random subset of 20% of all SPH particles onto the orbital (x-y) plane are shown at various times. The orbital motion is counter-clockwise. Units are such that $G = M = R = 1$, where M and R are the mass and radius of a single, spherical NS. Time has been shifted so that the maximum gravity wave luminosity occurs at $t = 20$.

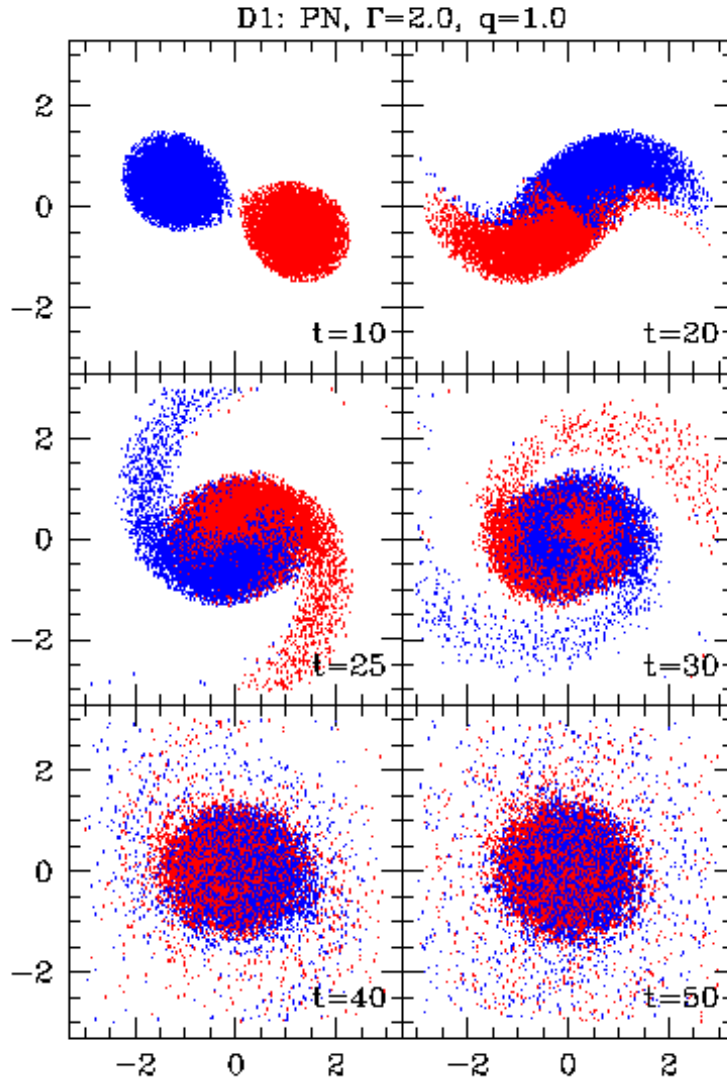


FIG. 2. Evolution of the system for Run D1, with $\Gamma = 2$ and $q = 1$. Here, all 1PN and 2.5PN corrections are included in the calculation. Conventions are as in Fig. 1.

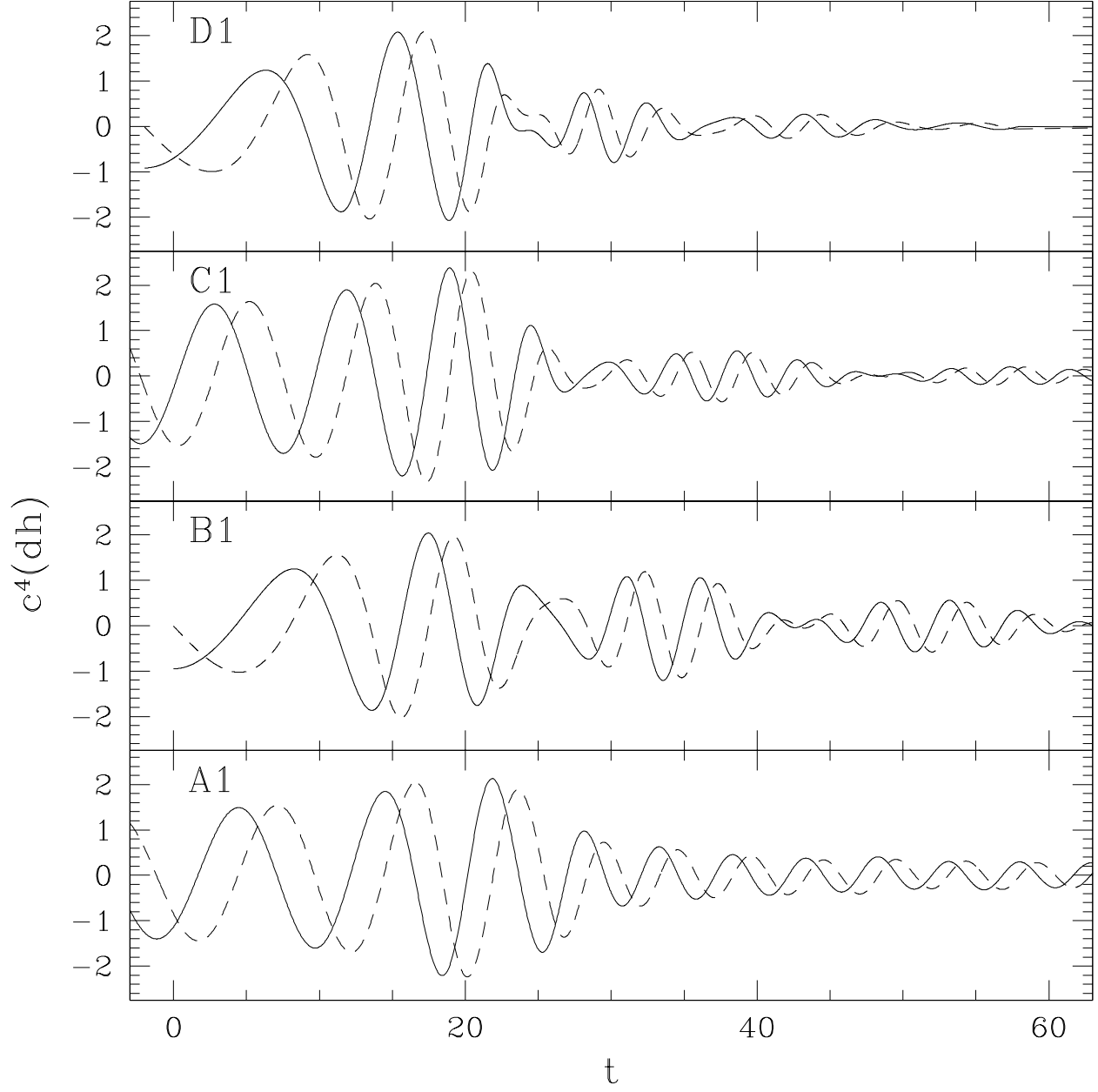


FIG. 3. Gravity wave signatures for the runs A1 (N, $\Gamma = 3$), B1 (PN, $\Gamma = 3$), C1 (N, $\Gamma = 2$), and D1 (PN, $\Gamma = 2$). All have $q = 1$. The solid line shows the h_+ polarization, the dashed line the h_\times polarization, both calculated for an observer at a distance d along the rotation axis. Note that at $t \gtrsim 60$, there is essentially no gravitational radiation given off by $\Gamma = 2$ EOS binaries.

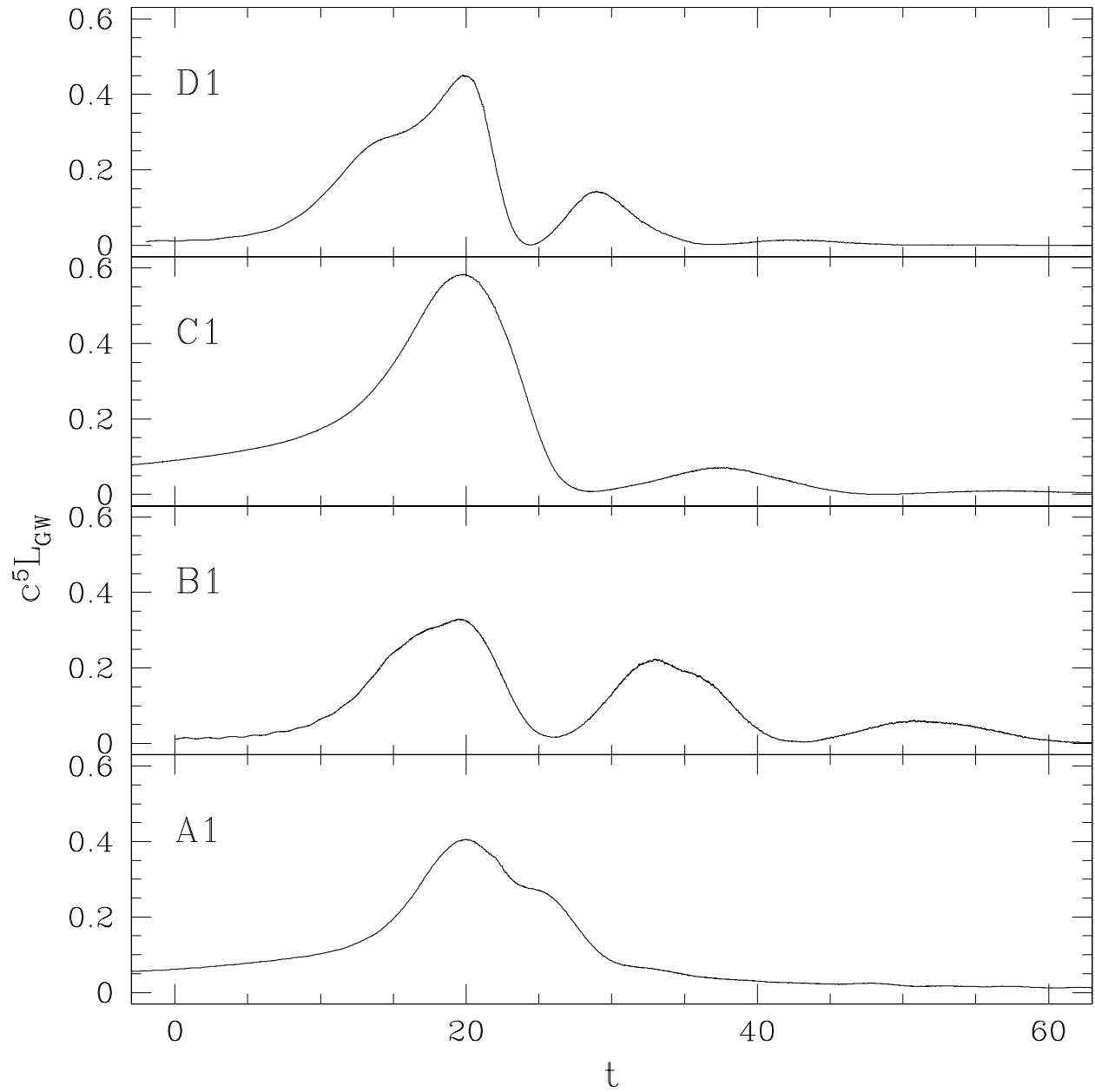


FIG. 4. Gravity wave luminosity for the same runs as in Fig. 3. We see clear evidence for a second gravity wave luminosity peak in both $\Gamma = 2$ runs, but only in the PN $\Gamma = 3$ run.

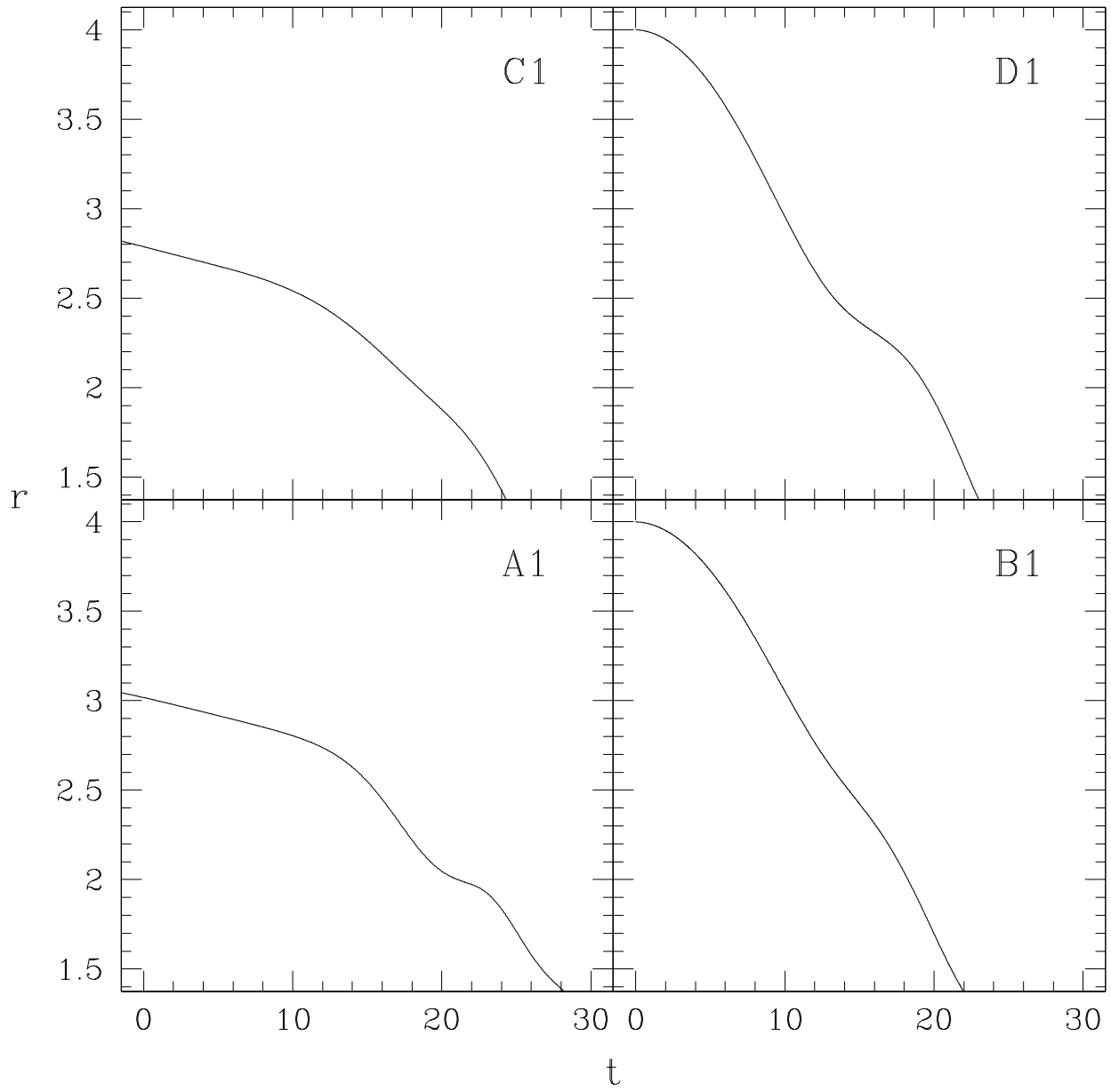


FIG. 5. Binary separation r for the same runs as in Fig. 3.

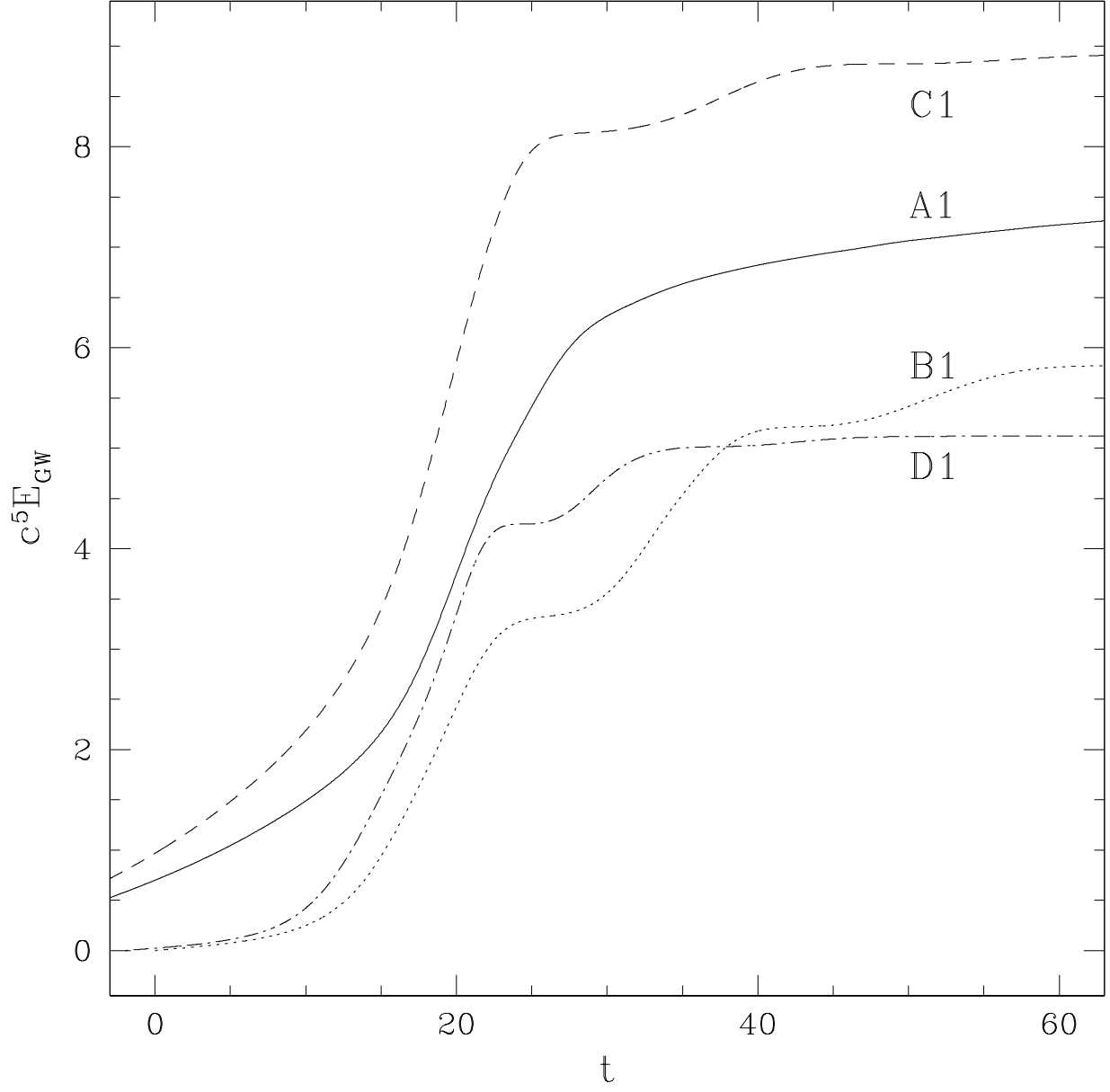


FIG. 6. Energy lost to gravitational radiation for the same runs shown in Figs. 3–5.

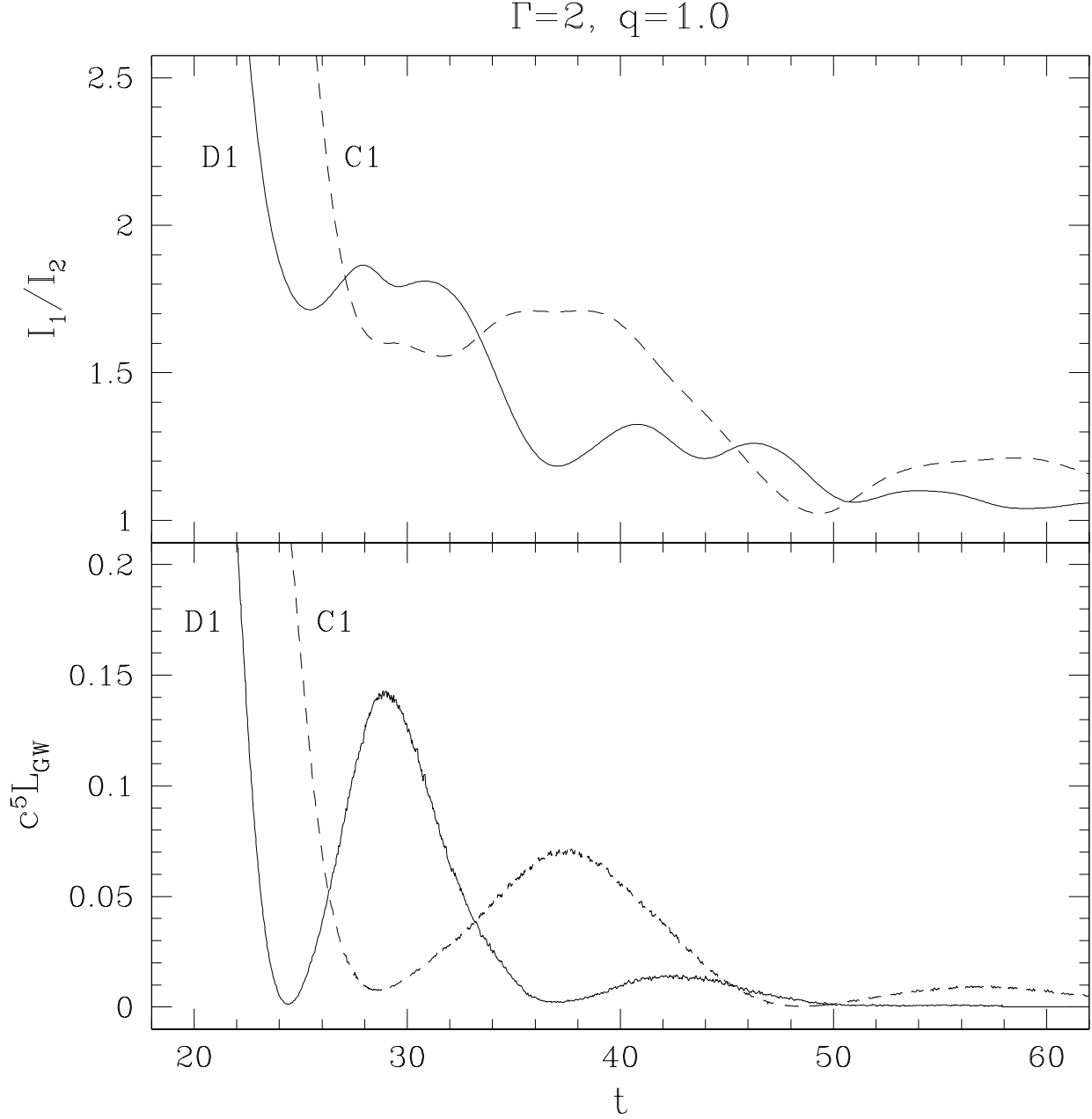


FIG. 7. Ratio of the principal moments of inertia in the equatorial plane for the remnants of runs C1 (N, $\Gamma = 2$; dashed lines) and D1 (PN, $\Gamma = 2$; solid lines), compared to the corresponding gravity wave luminosities at late times. We see a clear correlation between the two quantities, as the remnants relax towards an axisymmetric, oblate configuration. Here the remnants are defined by the density cut $r_* > 0.04$, which includes the entire binary initially, but only the inner part of the merger at later times.

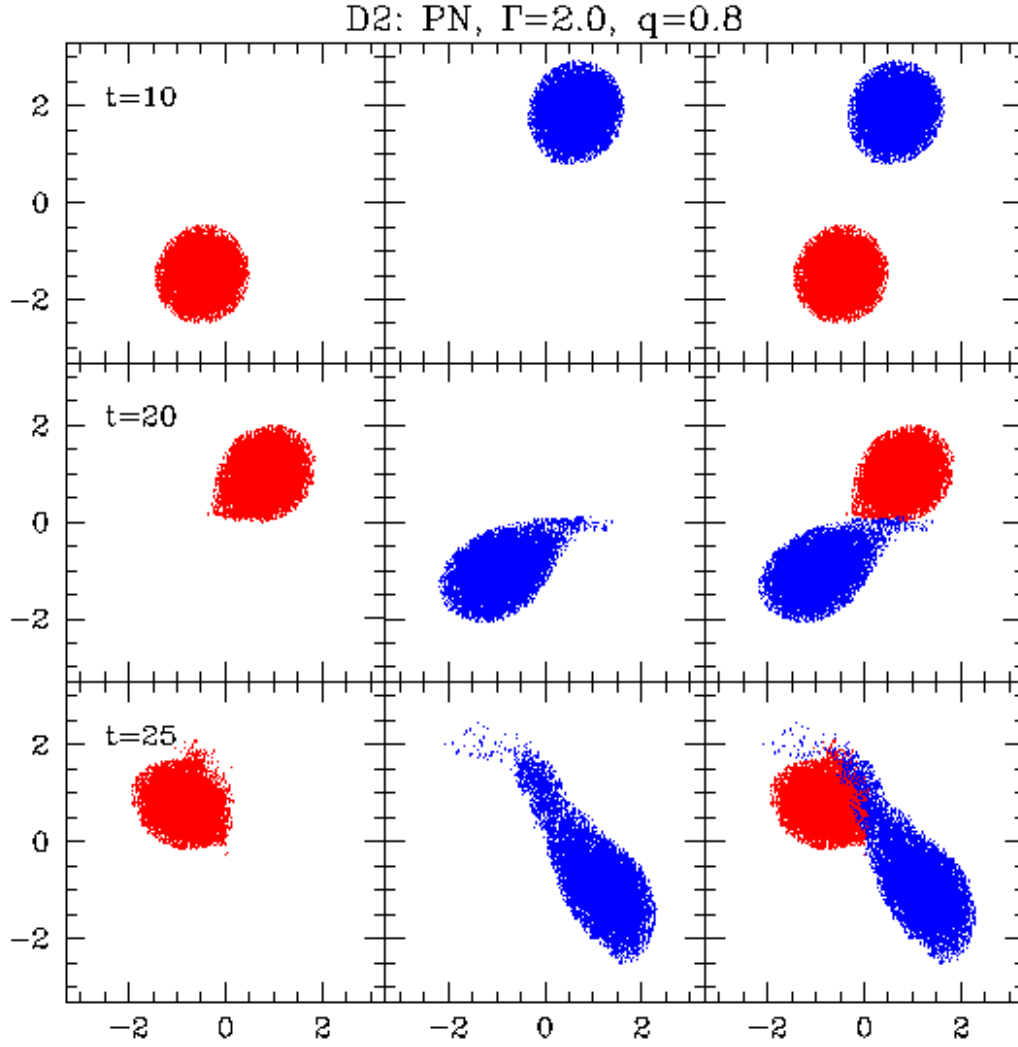


FIG. 8. Evolution of the system for run D2 with $\Gamma = 2$, $q = 0.8$, and 1PN corrections included. Projections of a random subset of 20% of all SPH particles onto the orbital (x-y) plane are shown at various times. Panels on the left show the primary, center panels show the secondary, and panels on the right the entire system.

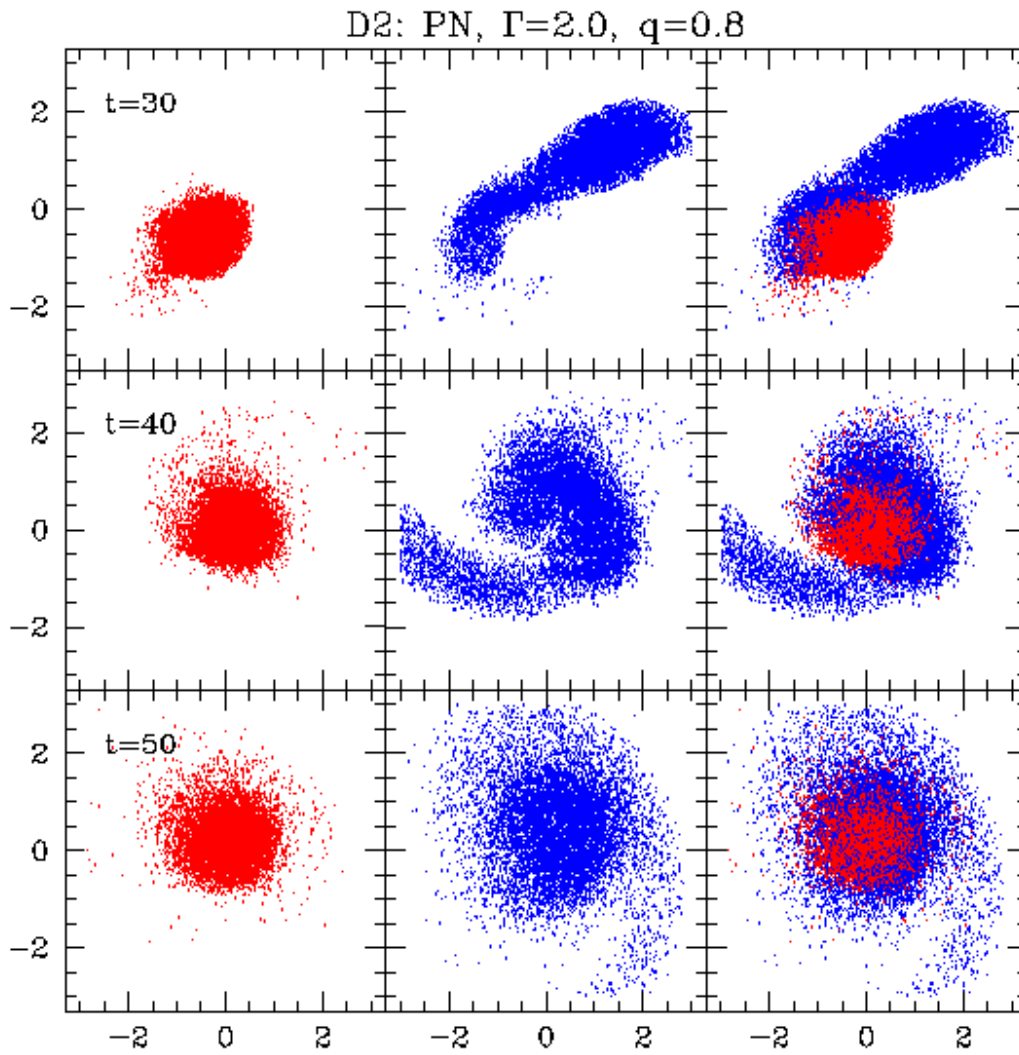


FIG. 9. Evolution of run D2, continued.

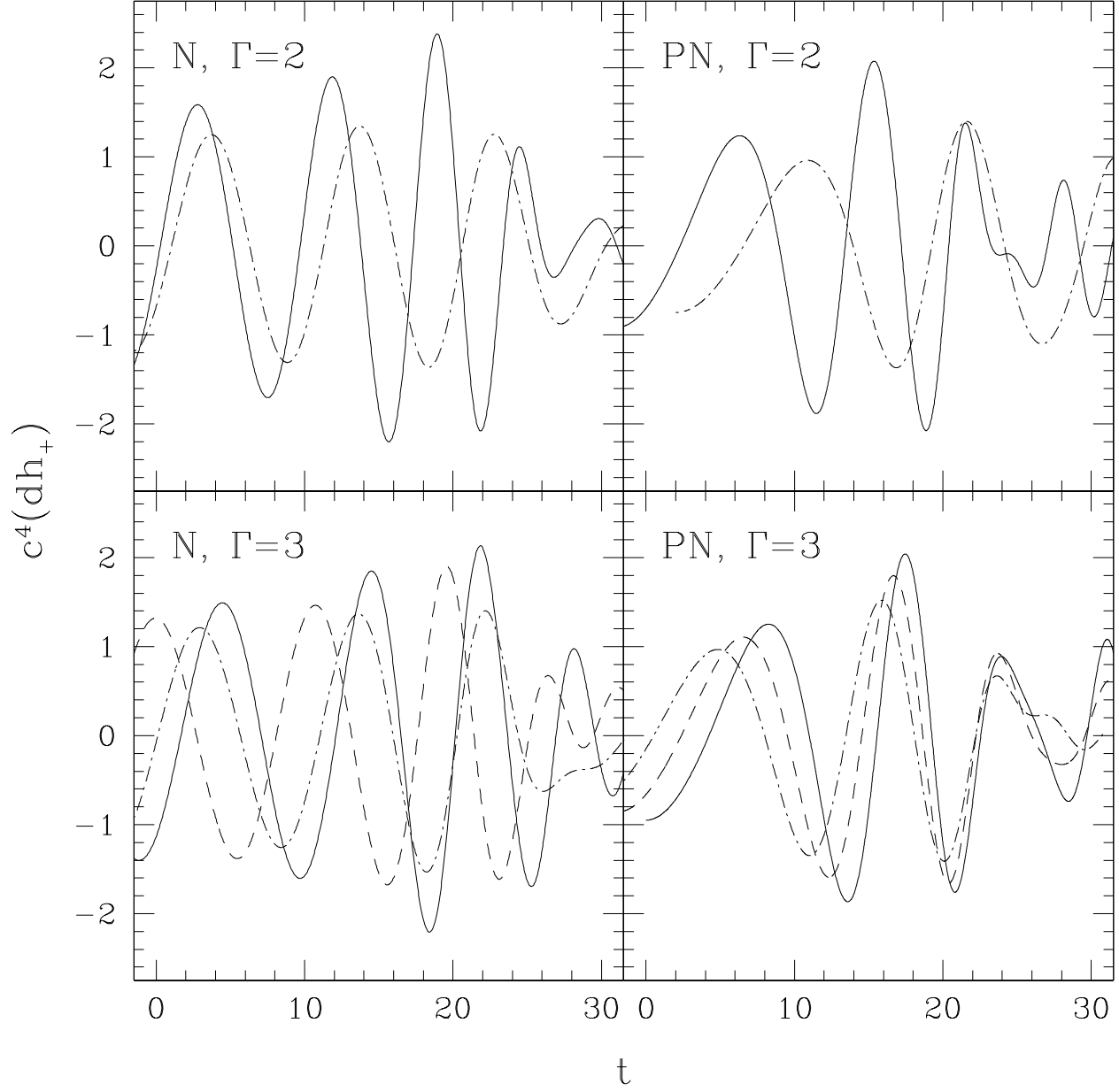


FIG. 10. Gravity wave amplitude h_+ for an observer located at a distance d along the rotation axis, comparing systems with different mass ratios. The solid lines correspond to $q = 1$, the dashed lines to $q = 0.9$, and the dot-dashed lines to $q = 0.8$.

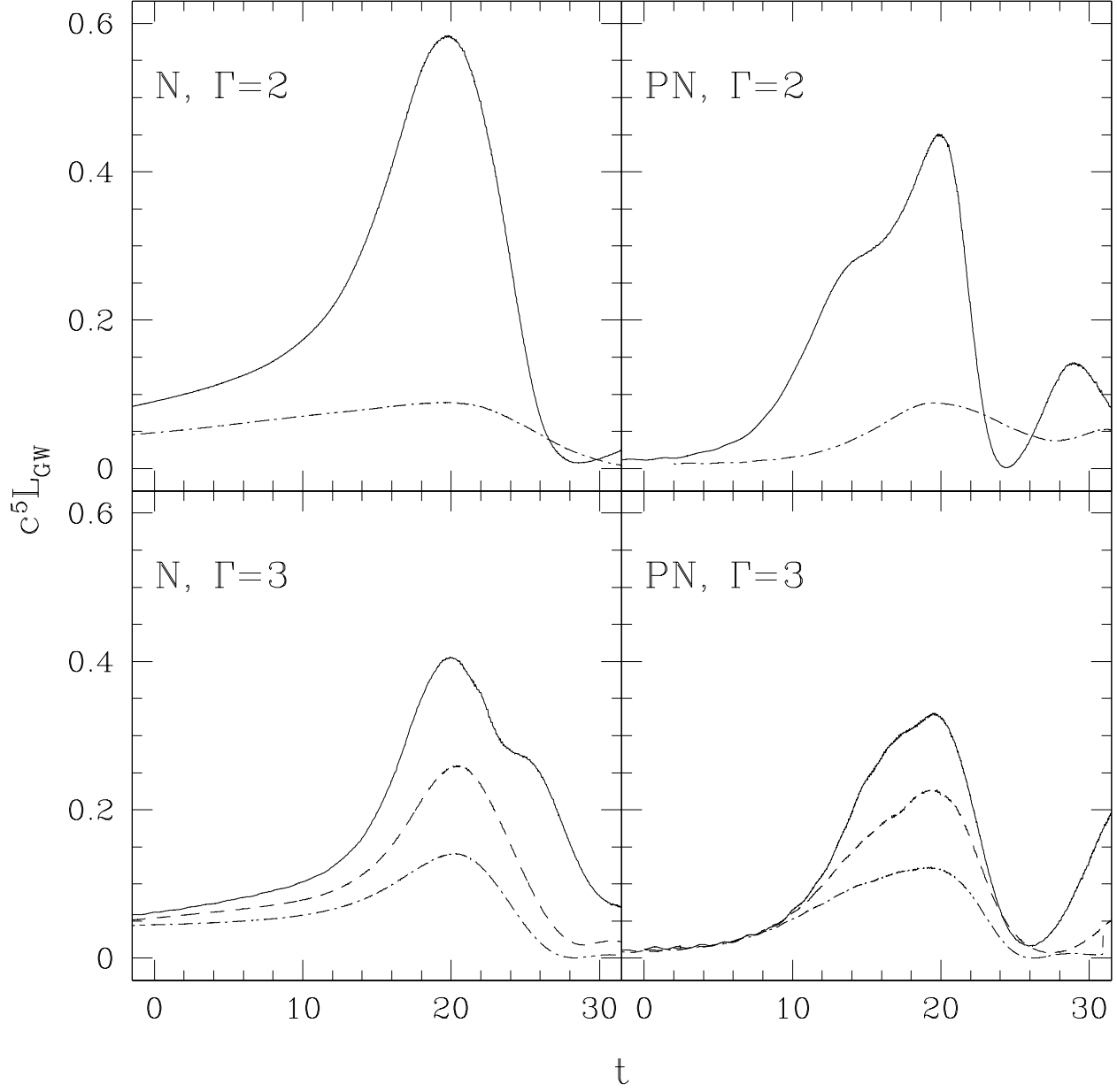


FIG. 11. Gravity wave luminosity for the same runs shown in Fig. 10. Conventions are in Fig. 10.

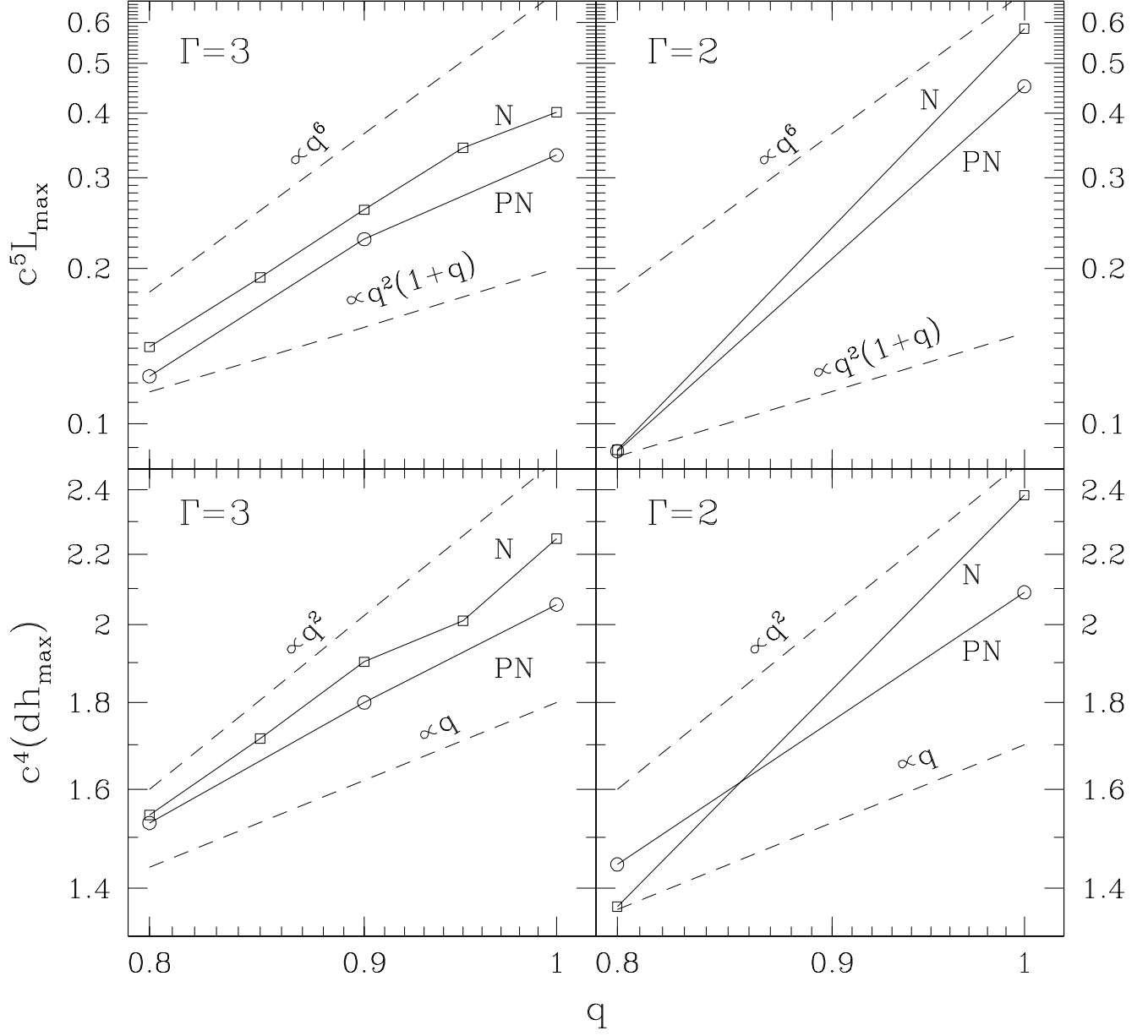


FIG. 12. Dependence of the maximum gravity wave amplitude and luminosity on the mass ratio (for all the synchronized binaries). The Keplerian point mass approximation gives $h_{\max} \propto q$ and $L_{\max} \propto q^2(1+q)$. Instead, the strictly Newtonian hydrodynamic calculations of RS2 give approximate power laws $h_{\max} \propto q^2$ and $L_{\max} \propto q^6$ for nearly equal-mass binaries containing $\Gamma = 3$ polytropes. Note that both axes are plotted logarithmically.

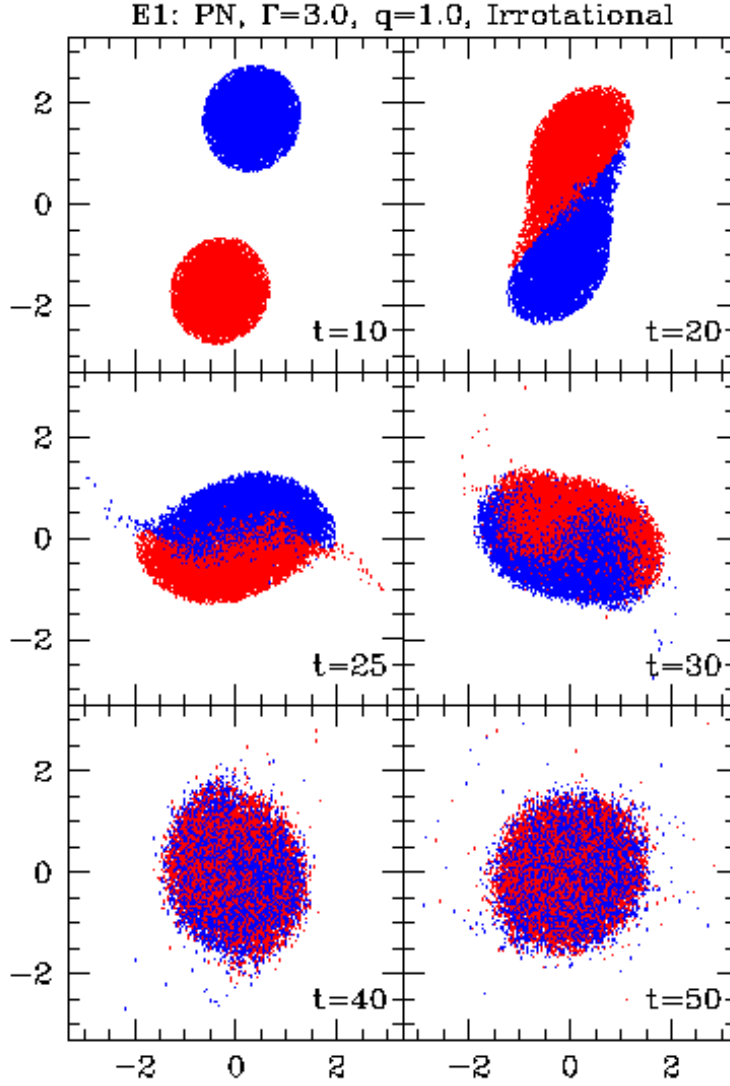


FIG. 13. Evolution of the $\Gamma = 3$, $q = 1$ irrotational binary system (E1). Conventions are as in Fig. 1. We see evidence for spiral arms forming after the initial merger, but containing much less mass than in the synchronized case. Note also that a longer time is required after merger to relax to a triaxial configuration.

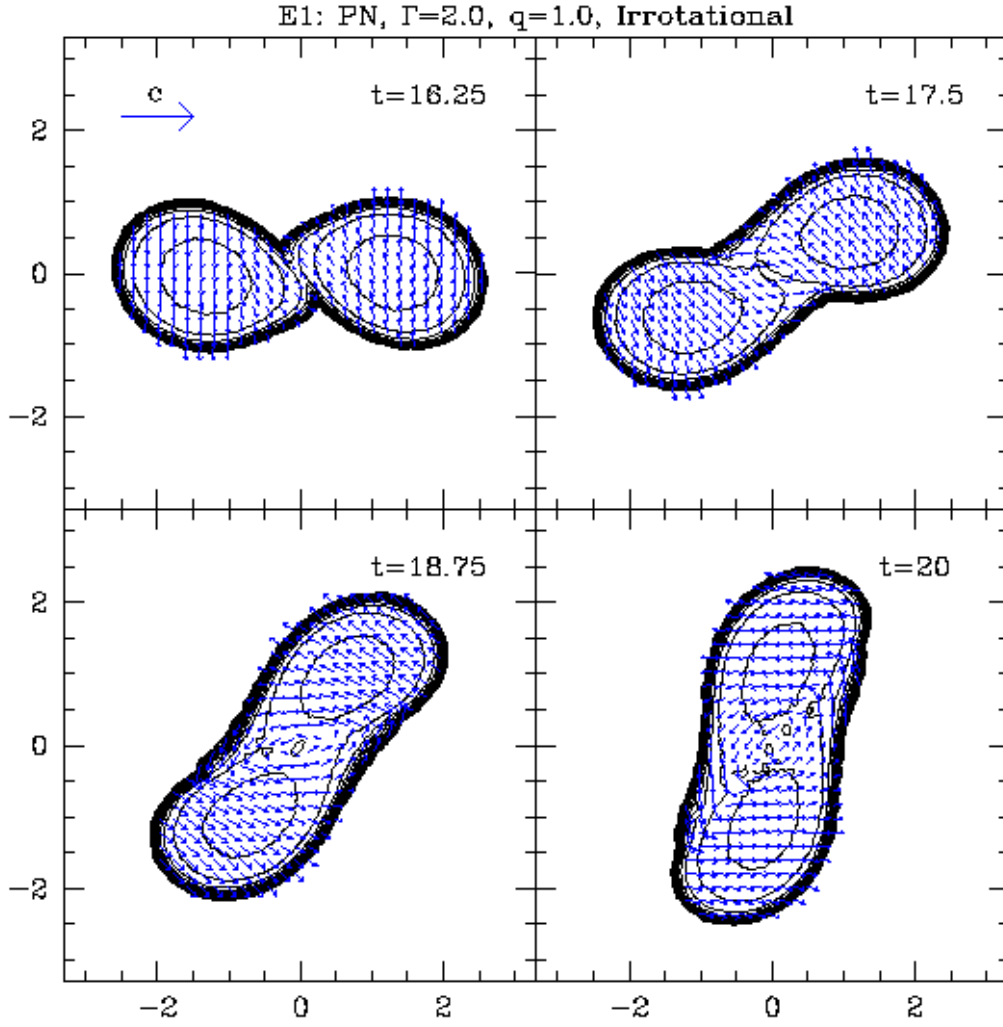


FIG. 14. Density contours and velocity field for the irrotational system in run E1. Density contours are spaced logarithmically, 4 per decade. The velocity field is shown in the *inertial frame*. A vector representing the speed of light ($c = c_{2.5PN}$, the physical value) is shown for comparison.

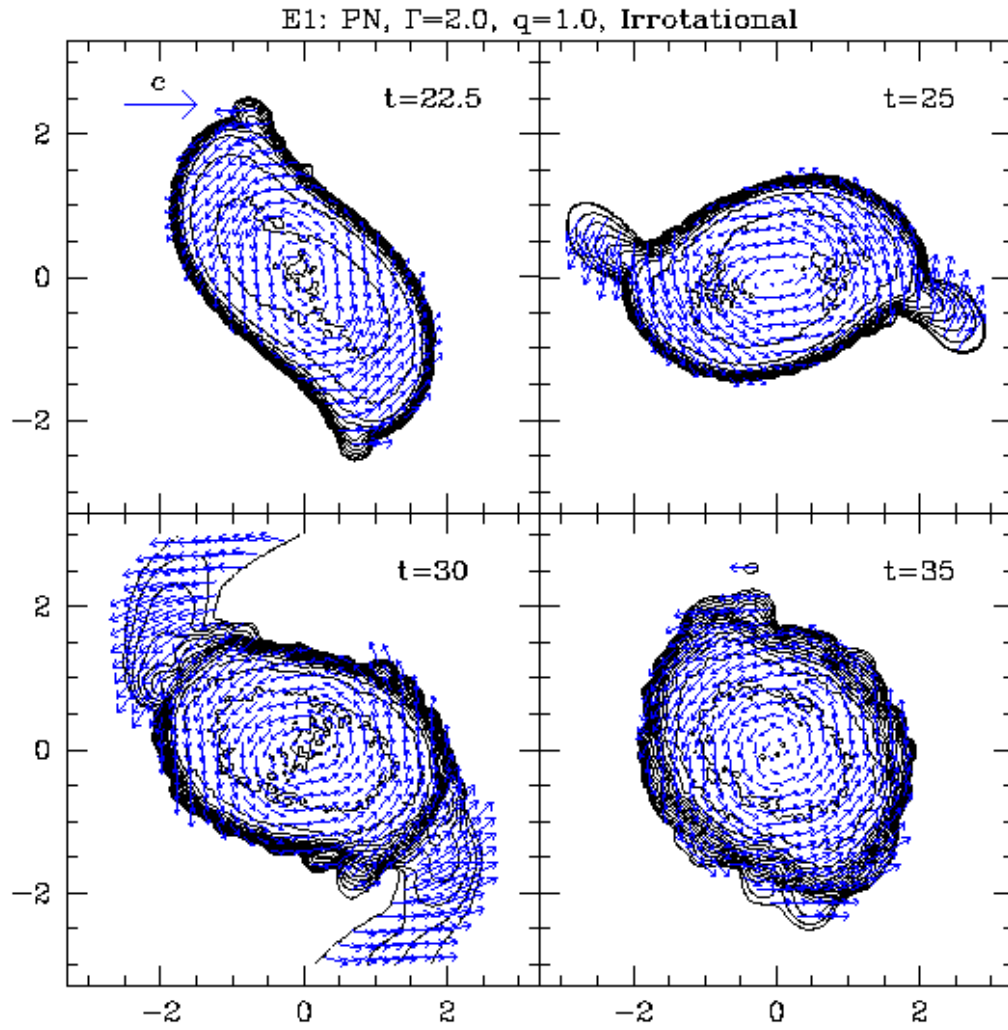


FIG. 15. Density contours and velocity field for run E1, continued.

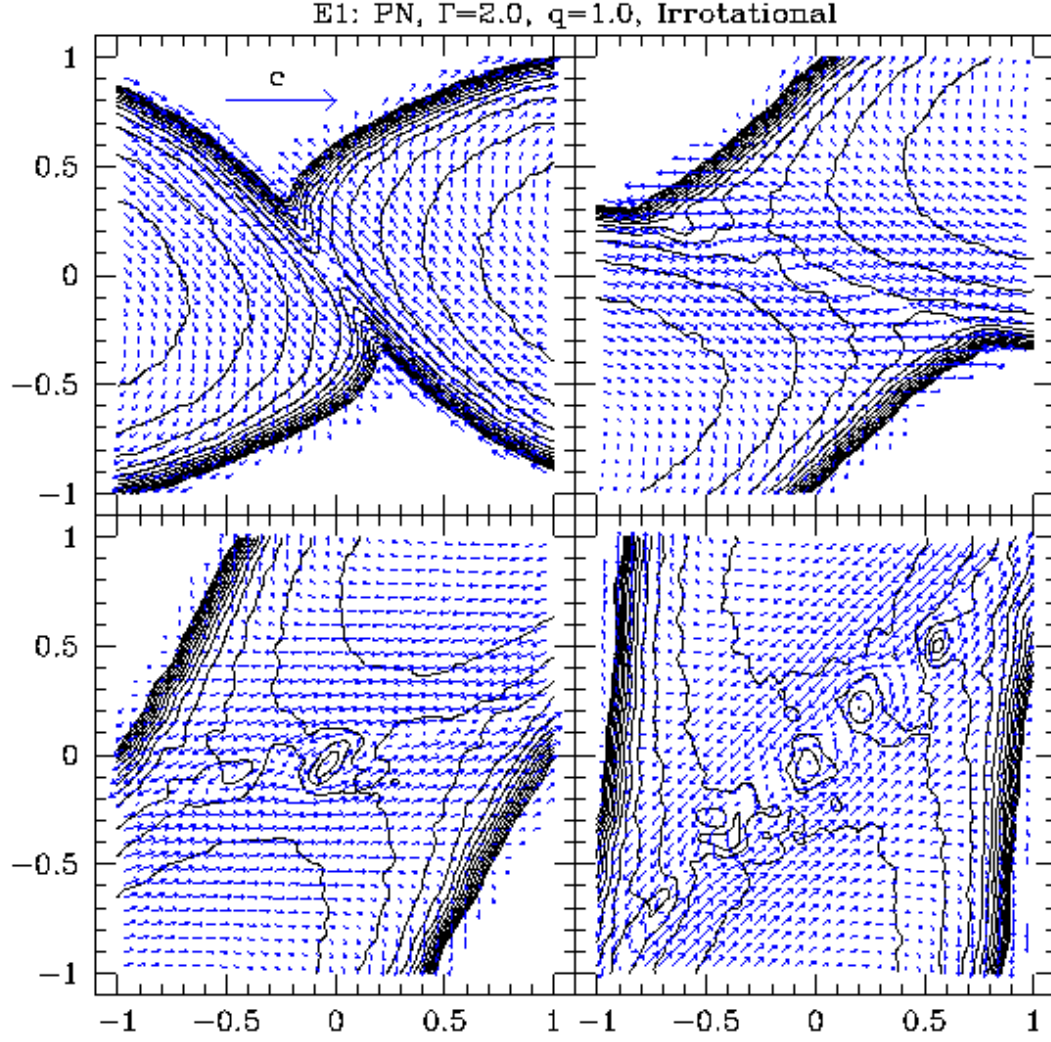


FIG. 16. Density contours and velocity field for the irrotational system in run E1, here focusing on the inner region of the merger. Panels correspond to the same times as shown in Fig. 14. Density contours are spaced logarithmically, 8 per decade. The velocity field is shown in the *corotating frame*, as defined by Eq. 4. As the surfaces of the two stars come into contact, they form an vortex sheet which extends over the full length of the interface.

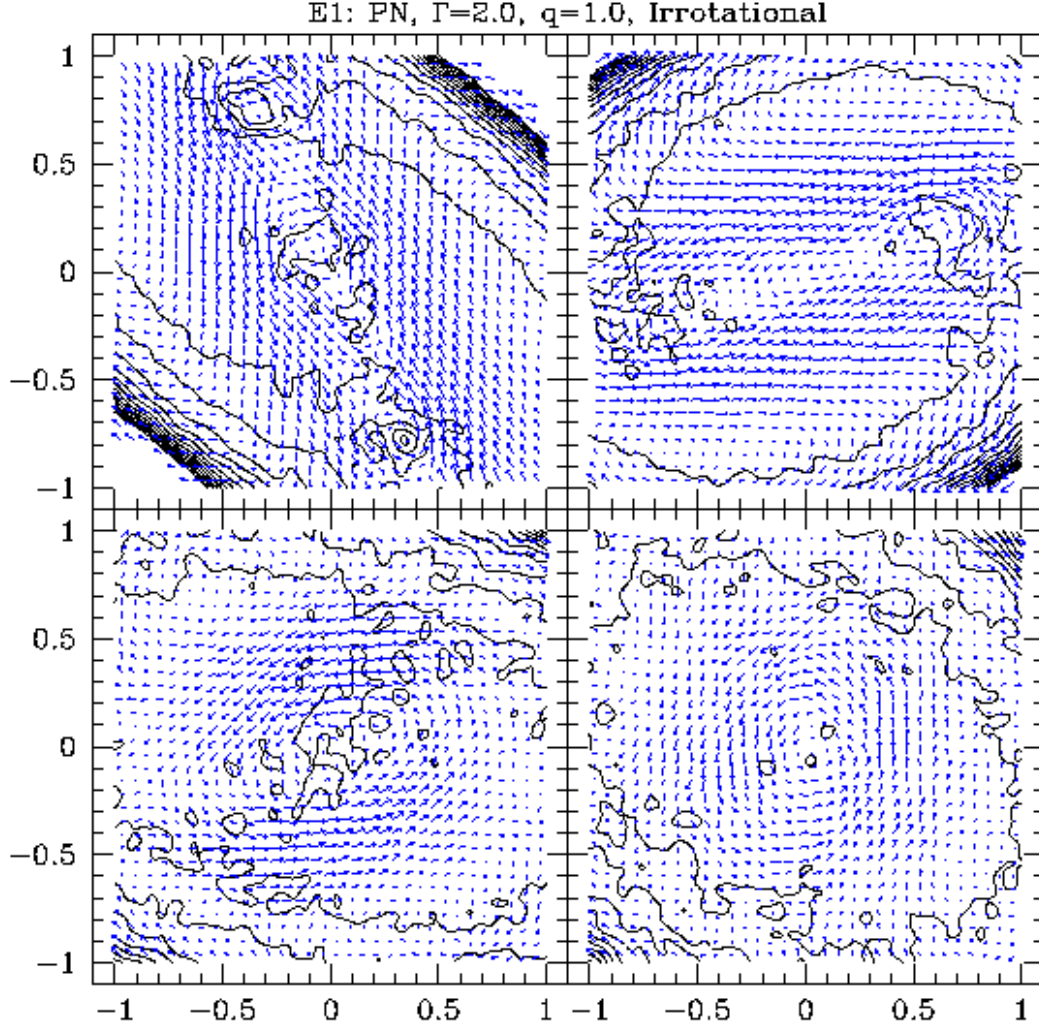


FIG. 17. Density contours and velocity field in the inner region for run E1, continued. Panels correspond to the same times as in Fig. 15.

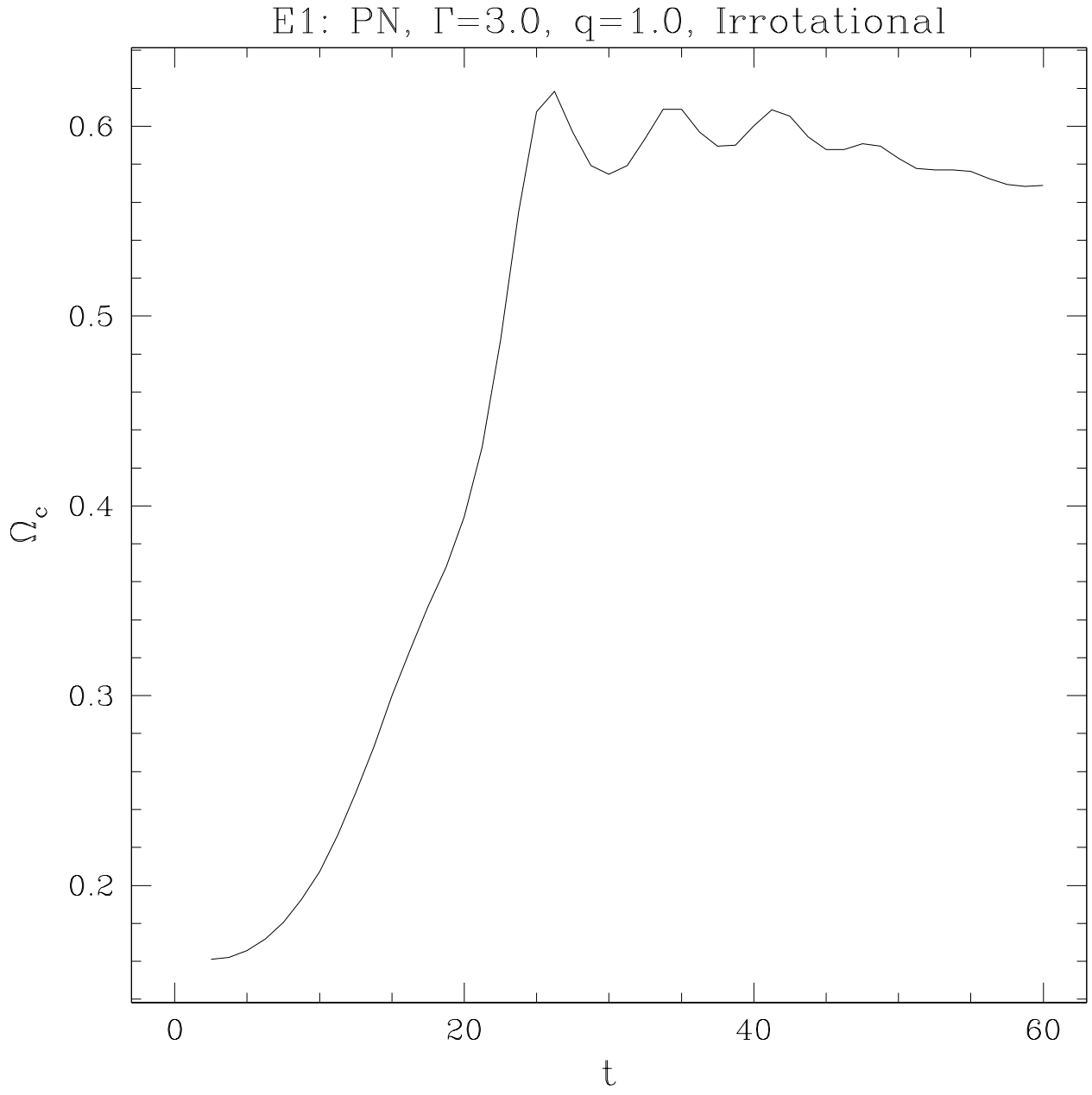


FIG. 18. Evolution of the mean angular velocity of the corotating frame Ω_c for run E1 (as defined by Eq. 4).

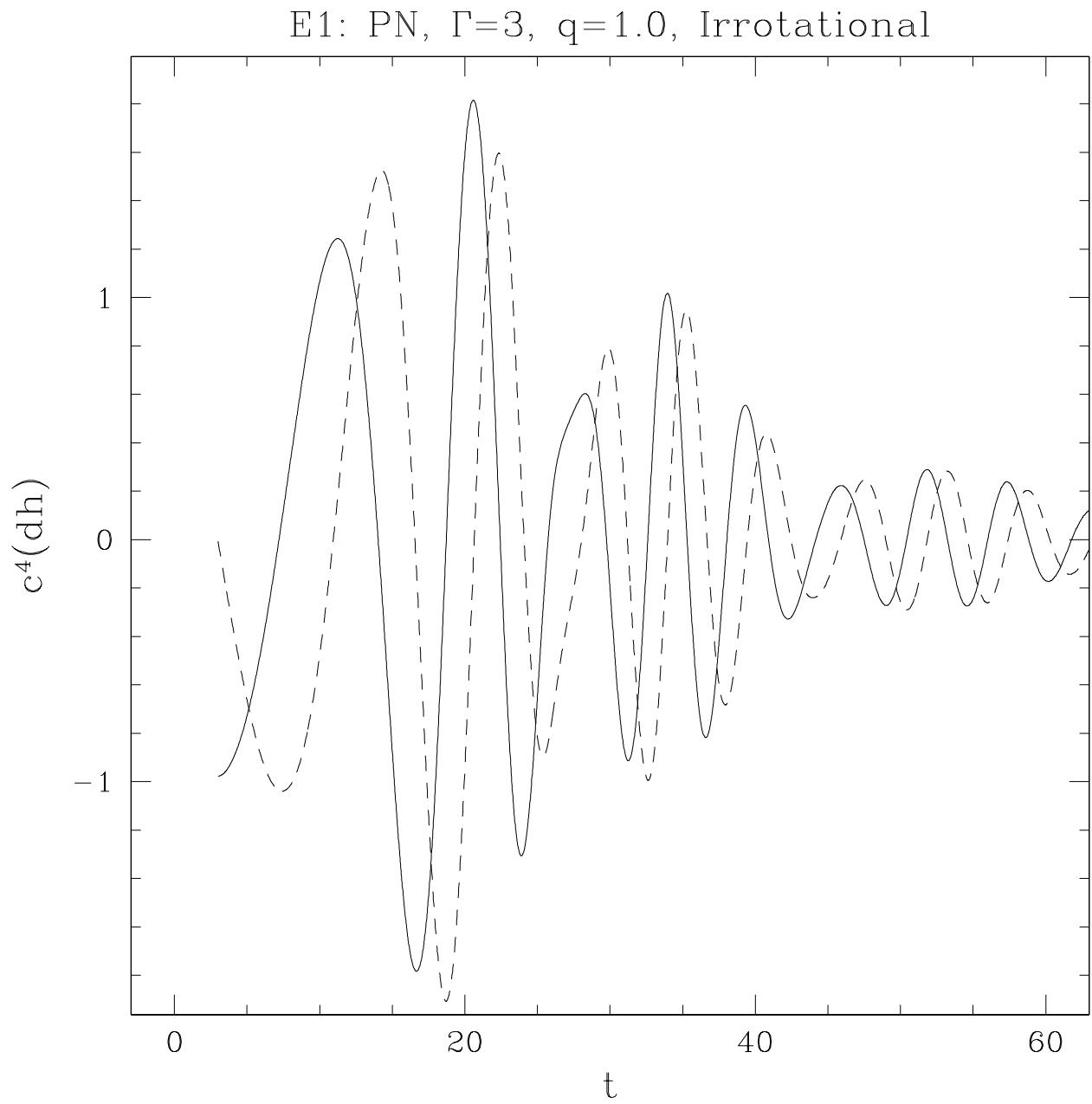


FIG. 19. Gravity wave signal for the run E1 (irrotational). Conventions are as in Fig. 3.

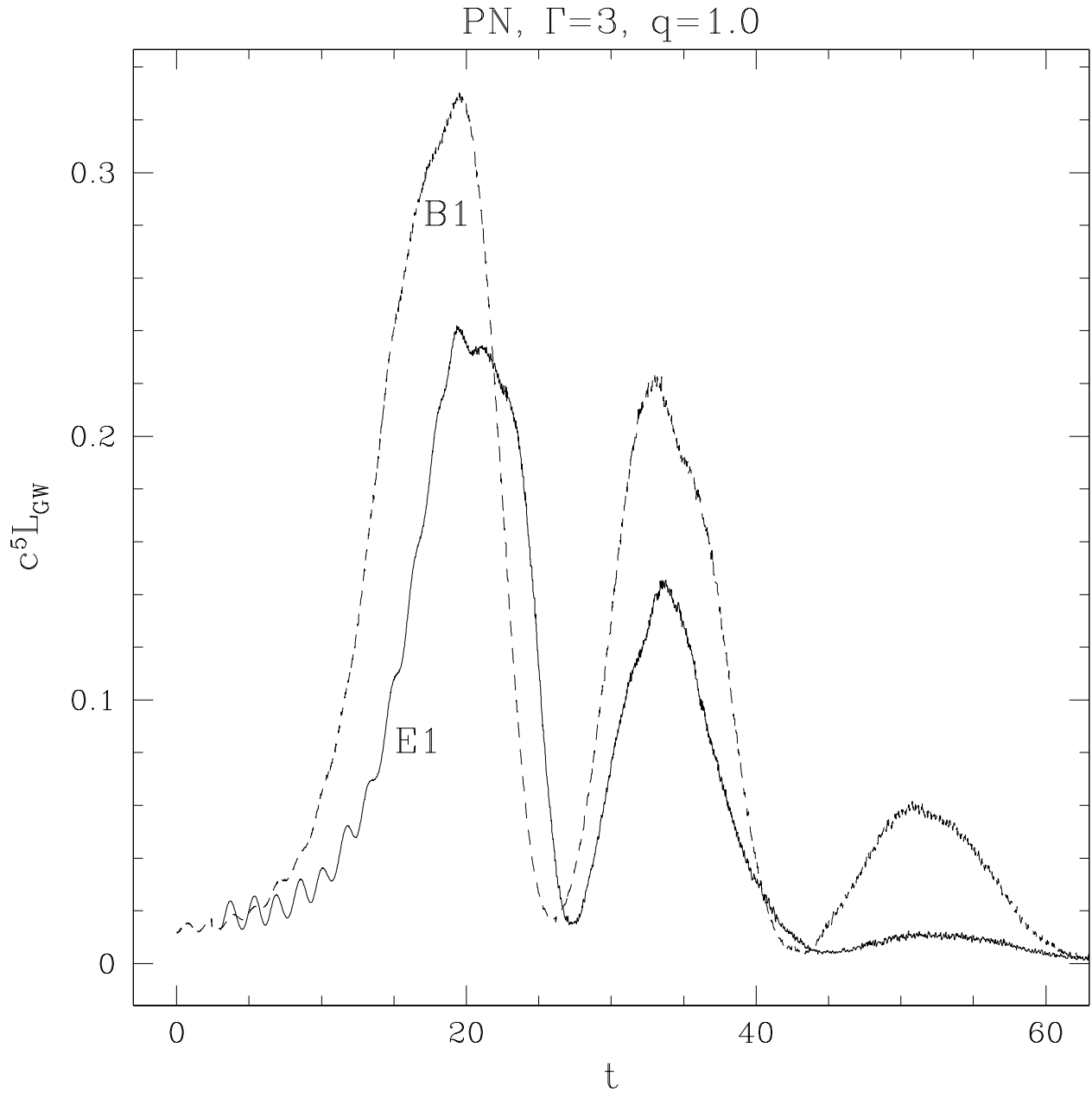


FIG. 20. Gravity wave luminosity for run E1 (irrotational) compared with that of run B1 (with a synchronized initial condition). Both runs include 1PN corrections, and have $\Gamma = 3$ and $q = 1$.

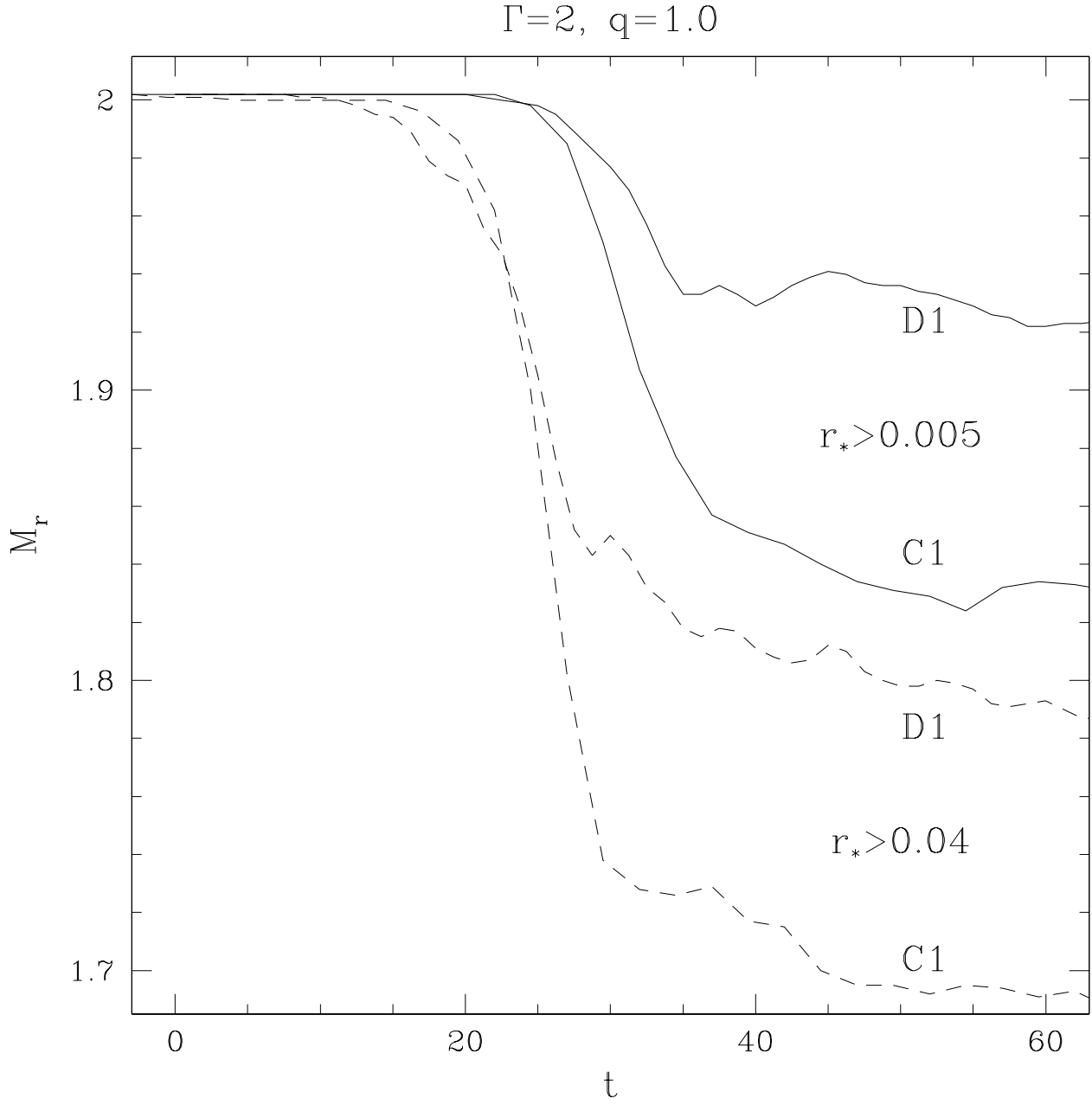


FIG. 21. Evolution of the remnant mass for the $\Gamma = 2, q = 1$ runs (C1 and D1). Suppression of mass shedding in the PN case leads to a higher final remnant mass. The density cut $r_* > 0.04$, shown as dashed lines, includes the inner remnant only. The cut $r_* > 0.005$, shown as solid curves, extends further into the outer halo.

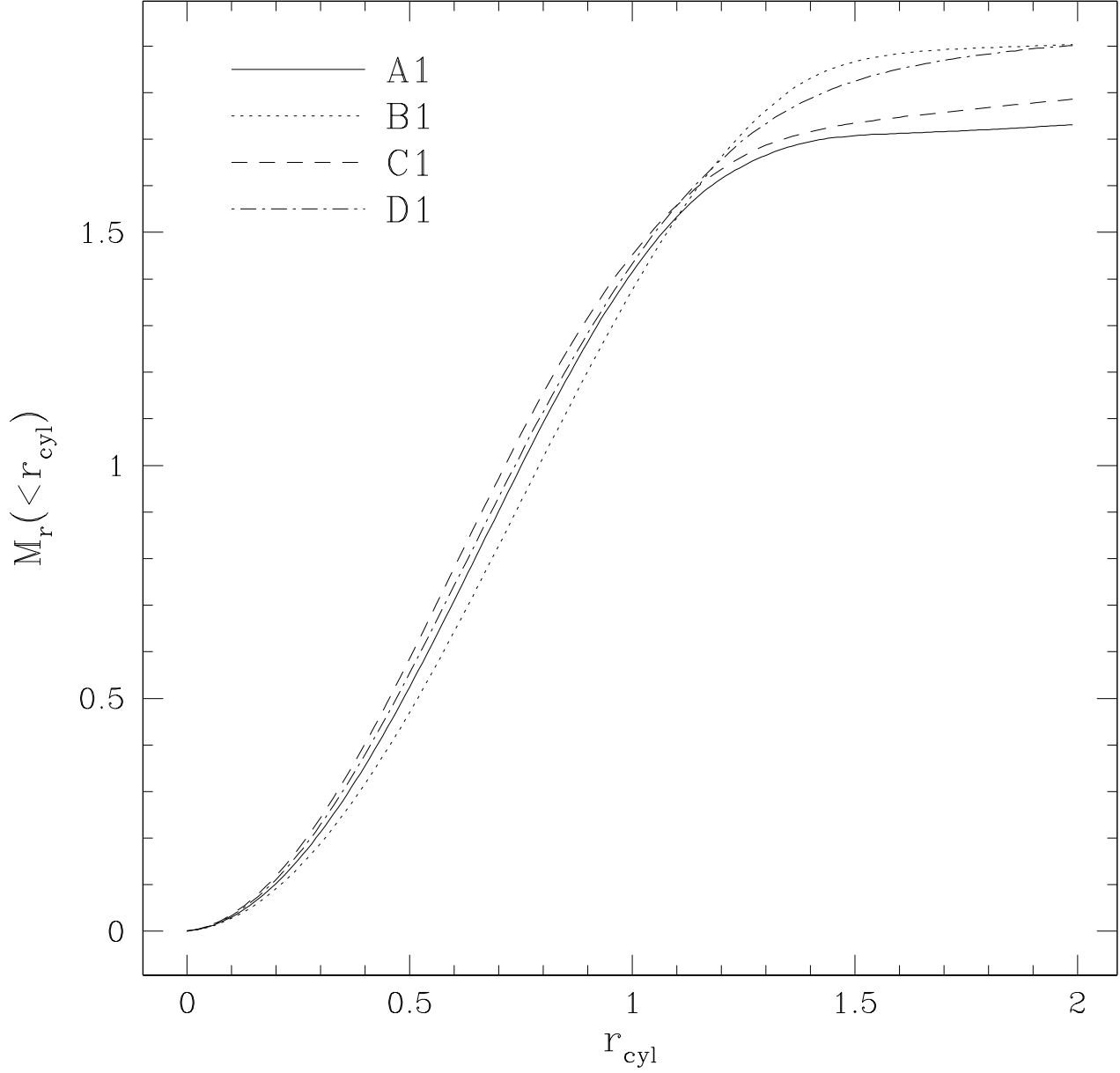


FIG. 22. Radial mass profiles of the final merger remnants in runs A1, B1, C1 and D1 (at $t = 60$). Here r_{cyl} is the distance from the rotation axis. We see that the internal structure is governed primarily by the EOS, with the $\Gamma = 2$ models slightly more centrally condensed than the $\Gamma = 3$ models, although 1PN effects do decrease the enclosed mass at small radii. At larger radii, we find more mass contained in the PN remnants, since much less mass has been ejected through spiral arms.

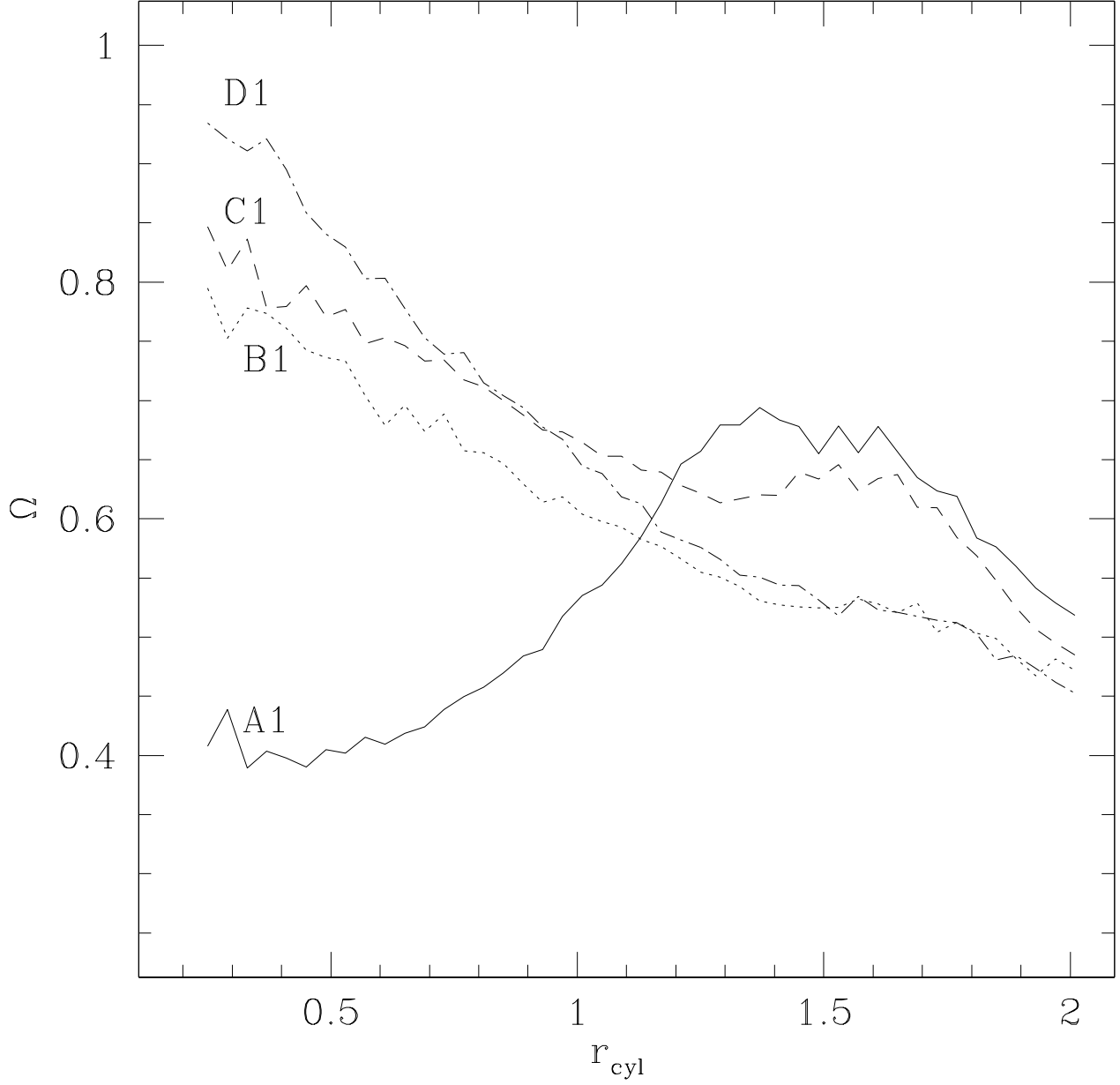


FIG. 23. Angular velocity profiles for the same merger remnants shown in Fig. 22. We see that all are differentially rotating, and all but the Newtonian $\Gamma = 3$ remnant show a decrease in angular velocity with increasing radius for $r_{\text{cyl}} \lesssim 1.3$. In general, at larger radii, the PN models show slower rotation, regardless of the EOS.

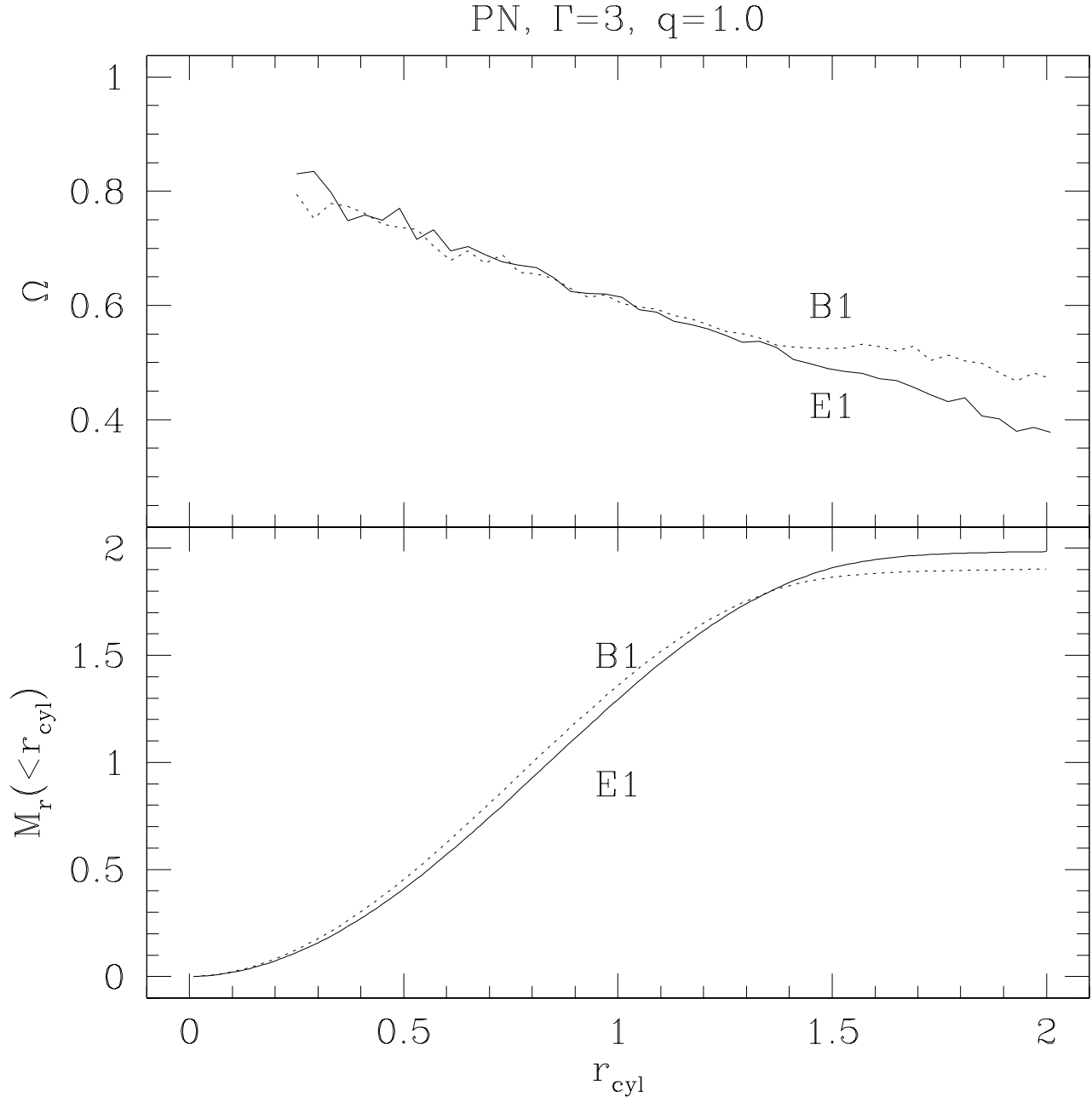


FIG. 24. Comparison of the merger remnants from runs B1 (synchronized initial condition) and E1 (irrotational initial condition). Both runs have $\Gamma = 3$ and 1PN corrections. Both the mass profiles and the rotation profiles of the inner remnants appear to be rather independent of the initial NS spins.

TABLE I. Properties of the $\Gamma = 2$ polytropic NS sequence. Units are defined such that $G = M = R = 1$. The polytropic constant k is defined by $P = kr_*^\Gamma$, and k_N is the Newtonian value, which is used in the Lane-Emden equation. The central density $(r_*)_c$ is in units of M/R^3 , while the central pressure ratio $(P/r_*c^2)_c$ and central gravitational potential ratio $(U_*/c^2)_c$ are dimensionless.

$1/c^2$	k/k_N	$(r_*)_c$	$(P/r_*c^2)_c$	$(U_*/c^2)_c$
$\Gamma = 2$				
0.01	1.202	0.6549	0.0050	0.0187
0.02	1.260	0.6670	0.0107	0.0376
0.03	1.308	0.6963	0.0174	0.0571
0.04	1.375	0.7173	0.0251	0.0767
0.05	1.439	0.7490	0.0343	0.0968

TABLE II. Properties of the PN polytropic models for NS of varying masses. Here the equation of state remains fixed for a given adiabatic index. All models have $1/c^2 = 0.05$. Quantities are defined as in Table I.

M	R	$(r_*)_c$	$(P/r_*c^2)_c$	$(U_*/c^2)_c$
$\Gamma = 2, k/k_N = 1.439$				
1.0	1.0	0.7490	0.0343	0.0968
0.8	1.025	0.5311	0.0243	0.0747
$\Gamma = 3, k/k_N = 1.918$				
1.0	1.0	0.4051	0.0397	0.0813
0.9	0.986	0.3781	0.0349	0.0757
0.8	0.969	0.3501	0.0299	0.0683

TABLE III. Selected quantities from each of the simulations. Note that only runs A1, B1, C1, D1, D2 and E1 were extended until a stable final remnant was formed. All other runs were terminated shortly after the first gravity wave luminosity peak. Here t_0 is the time at which the run was started (see Sec. II C), and θ_{lag} is the lag angle at first contact, given for both NS (see Sec. III). Quantities involving the first and second gravity wave luminosity peaks are labeled with superscripts (1) and (2). All SPH particles with $r < 2.0$ are used to calculate the final rest mass M_r , gravitational mass M_{gr} , and Kerr parameter a_r of the final remnant (at $t = 60$; see Sec. III D).

Run	q	t_0	$\theta_{\text{lag}}(\text{deg})$	$c^5 L_{GW}^{(1)}$	$c^4(dh_{\text{max}}^{(1)})$	$c^5 L_{GW}^{(2)}$	$c^4(dh_{\text{max}}^{(2)})$	$t_{\text{max}}^{(2)}$	M_r	M_{gr}	a_r
N, $\Gamma = 3.0$, Synchronized, $r_0 = 3.1$											
A1	1.00	-13	4.2	0.4061	2.2469	0.0615	0.6421	33	1.730	N/A	0.469
A2	0.95	-15	3.0, 3.5	0.3284	2.0505						
A3	0.90	-18	3.0, 3.7	0.2617	1.8439						
A4	0.85	-22	3.0, 4.8	0.2045	1.6545						
A5	0.80	-27	3.0, 5.0	0.1567	1.4850						
PN, $\Gamma = 3.0$, Synchronized, $r_0 = 4.0$											
B1	1.00	0	11.2	0.3317	2.0549	0.2253	1.2129	33	1.902	1.847	0.716
B2	0.90	-2	10.3, 11.1	0.2280	1.7999						
B3	0.80	-4	9.1, 12.1	0.1216	1.5291						
N, $\Gamma = 2.0$, Synchronized, $r_0 = 2.9$											
C1	1.00	-13	4.0	0.5837	2.3830	0.0721	0.5668	38	1.785	N/A	0.590
C2	0.80	-13	5.1, 11.5	0.0891	1.3635						
PN, $\Gamma = 2.0$, Synchronized, $r_0 = 4.0$											
D1	1.00	-2	11.0	0.4510	2.0890	0.1442	0.8258	29	1.900	1.747	0.832
D2	0.80	2	5.2, 10.1	0.0885	1.4456	0.0530	1.0896	31	1.646	1.529	0.822
PN, $\Gamma = 3.0$, Irrotational, $r_0 = 4.0$											
E1	1.00	3	14.5	0.2419	1.9093	0.1475	1.0200	33	1.983	1.913	0.765